Raman Scattering in Semiconductor Nanostructures

—— Heterostructures and Nanocrystals

by

Aishi Yamamoto

Submitted in partial fulfillment of requirements for the degree of

Doctor of Philosophy (Science) in Doctoral Program in

University of Tsukuba

January, 1993

ABSTRACT

Raman scattering in low-dimensional semiconductor nanostructures, especially heterostructures and nanocrystals, were studied. We used ZnSe–ZnS strained-layer superlattices (SLSs), $Si_{0.5}Ge_{0.5}/Ge/Si_{1-x}Ge_x$ heterostructures, and Si nanocrystals. By using macro– and micro–Raman scattering measurement techniques, zone–folded modes of acoustic phonons, stress effect on the optical phonons, and the confinement of optical phonons were studied. These phenomena are peculiar to the semiconductor nanostructures.

We first showed higher–order zone–folded phonon modes, up to the 5th order, in ZnSe–ZnS strained–layer superlattices (SLSs) whose average lattice constant is equal to that of GaAs substrate. We were able to reproduce our zone–folded spectrum using transmission electron microscopy (TEM) data and a photoelastic model. The agreement between our calculation and the measurement shows that the Raman spectrum reflects dominantly the periodicity of the superlattices and the roughness of the interface. Furthermore, the stress does not play an important role to the observation of the zone–folded modes.

Next, we studied the optical phonons in ZnSe–ZnS SLSs. In these heterostructures, there exists a strain lying in the plane parallel to the interface. In order to investigate the directional stress, we newly measured Raman scattering with the incident light parallel as well as perpendicular to the interface plane. As a result, we observed for the first time two types of the optical phonon shifts, a singlet and a doublet, induced by the biaxial stress.

We measured the Raman scattering from the submicron–order region of $Si_{0.5}Ge_{0.5}/Ge/Si_{1-x}Ge_x$ heterostructures. Generally, the spatial resolution is thought to be limited by the spot size of the laser beam at the sample surface. The spot size is about 1 μm when the micro–Raman measurement system is used. Whereas, we measured the Raman scattering in the heterostructures by scanning the irradiated spot at intervals of ~0.1 μm and obtained submicron–order profile of Raman spectra. The calculations which consider the beam profile and the structural profile fully reproduced the dependence of the Raman intensity on the position of the irradiated spot. The results suggest that if we consider the beam profile, we can observe the Raman signal from the submicron–order region of the opaque sample.

Finally, we studied the confinement effect of optical phonons in Si nanocrystals fabricated by a gas break–down method. The Raman spectra of the smallest nanocrystals showed high energy shift and the narrowing of the spectral width. These anomalous behaviors can be explained by the spatial correlation (SC) model which considers both the dispersion curves of LO and TO phonons. It was shown that as the size of nanocrystals decreases, the energy difference between LO and TO phonons increases, the LO phonon mode becomes broad and weak, and TO phonon mode becomes dominant. Our treatment of the confinement of optical phonons also reasonably explained the previous experimental results of the other authors.

In this work, we have discussed and clarified the phonon dynamics in semiconductor nanostructures.

TABLE OF CONTENTS

CHAPTER I

INTRODUCTION

In 1928, a new light scattering phenomenon was discovered by C. V. Raman.[1] The new phenomenon is nowadays called the "Raman effect." It was soon realized that the newly discovered effect constituted an excellent tool to study molecular structures. At the early stages, mercury arcs were used to excite the samples and it was difficult to adopt the experiments for lattice dynamics in single crystals because of the small scattering cross sections. The discovery of laser in 1960 changed this situation rather drastically. The laser is an ideal excitation light source for Raman scattering spectroscopy for its monochromaticity, coherence, collimation, and power. The detection technique also changed from photographic recording to photoelectronic recording with photon counting or optical multichannel analyzers. At present, several reviews of application of Raman spectroscopy to the investigation and characterization of semiconductor materials have appeared.[2–7]

Recently, optical and electronic properties of nanometer–size semiconductor structures (nanostructures) have attracted much attention, because they exhibit new quantum phenomena and have potentials for becoming novel and future devices. The development of crystal growth techniques like molecular beam epitaxy (MBE), metalorganic chemical vapor deposition (MOCVD), and metalorganic molecular beam epitaxy (MOMBE) made it possible to grow artificial nanostructures with dimensions comparable to the distance of a few monolayers. For example, much interest has been paid in wide–band–gap II–VI semiconductor heterostructures both for improved understanding of their physical properties and for their potential applications in optoelectronic devices in the blue spectral region.[8,9] Furthermore, very recently, unique optical properties of nanostructures (heterostructures, nanocrystals, etc.) made from indirect-gap semiconductors such Si, Ge, etc. have been reported.[10-14] In particular, the discovery of intense visible luminescence in nanocrystals of Si and Ge is an extremely important scientific breakthrough with enormous technological implications, since it opens a new possibility for group IV semiconductors as new materials for optoelectronic applications.

For fabricating a good quality sample, the structural characterizations of the nanostructures, such as periodicity and interface roughness in the superlattices and the crystallinity of the nanocrystals, are highly important. Most of the heterostructures have inherent stress at the heterojunction interface due to the lattice mismatch. These stress induces a change in the band structure, and then affect the optical properties.[15,16] Therefore, it is essentially important to evaluate the strains in the heterostructures.

Raman spectroscopy is a very useful tool to study lattice dynamics in semiconductor nanostructures as well as bulk semiconductors. Raman spectra offer various information on the stress in the heterostructures, the periodicity of the superlattices, the size of the nanocrystals, etc. Therefore, Raman spectroscopy is applicable to characterize the nanostructures. However, the quantitative characterization method has not been completely established, yet. Therefore, it is strongly desired to establish the nondestructive characterization method of the nanostructures.

From the fundamental viewpoint, a lot of interesting physical phenomena have been observed in the nanostructures. In the case of superlattices, new behaviors of phonons, such as the zone-folding of acoustic modes and the confinement of optical phonons, are being studied extensively.[6] In the case of nanocrystals, three-dimensional confinement of optical phonons,[17-22] surface phonons,[23-26] and new acoustic phonons[27] are currently under investigation.

As mentioned above, it is essentially important to study the Raman scattering in nanostructures both for improved understanding of lattice dynamics and for establishing the complete method of sample characterization. This thesis is devoted to the properties of phonons in the nanostructures —— heterostructures and nanocrystals —— by means of Raman scattering spectroscopy. Three issues were mainly studied: (a) zone-folded acoustic modes in ZnSe–ZnS strained-layer superlattices (SLSs), (b) effects of biaxial stress on optical phonon in ZnSe–ZnS SLSs, and (c) phonon confinements in Si nanocrystals. The construction of this thesis is as follows.

In Chapter II, theoretical treatments of Raman scattering processes and the preview of Raman scattering in nanostructures are described.

In Chapter III, the experimental equipments used in this thesis (macro- and micro-Raman measurement systems) are illustrated.

In Chapter IV, higher-order zone-folded modes of acoustic phonons in ZnSe–ZnS SLSs are studied. One previously speculates that the lattice mismatch makes it difficult to establish high-quality epitaxial layers and to observe zone-folded modes. Whereas, in this study we first showed the higher-order doublet phonon modes, up to the 5th order, in ZnSe–ZnS SLSs whose average lattice constant is equal to that of a GaAs substrate.[28] We tried to answer two questions. One is why such higher order folded modes were observed. The other is whether or not the stress is a matter of the zone folding of phonon modes. A model calculation based on the transmission electron microscopy (TEM) data was used to solve these problems.

In Chapter V, biaxial splitting of optical phonons in ZnSe–ZnS SLSs is shown. In these heterostructures, there exists a stress lying in the plane parallel to the interface. In this sense they have quasi–two–dimensional structures. The biaxial stress may induce the biaxial splitting of optical phonons. In order to find the biaxial splitting of the phonon modes, we for the first time measured Raman scattering with the incident light parallel as well as perpendicular to the interface plane. We demonstrated that two types of phonon modes, that is a singlet and a doublet, can be observed.

In Chapter VI, we study the Raman scattering from the submicron–order region of $Si_{0.5}Ge_{0.5}/Ge/Si_{1-x}Ge_x$ heterostructures. Generally, the spatial resolution of the Raman signal is thought to be limited by the spot size of the laser beam (~1 μm) at the sample surface.[29–31] Whereas, we were able to observe the submicron–order region of the heterostructure by scanning the irradiated spot at intervals of ~0.1 μm. It is suggested that when we take account of the beam profile, we can observe the Raman signal from the submicron–order region of the opaque sample.

In Chapter VII, a new treatment of the confinement effect on optical phonons in Si nanocrystals is proposed. Most of the nanocrystals studied in the previous works are embedded in glass matrices.[14,17,19,21,22,32] Therefore, extrinsic effects such as strain between nanocrystals and matrices can not be neglected. It is desirable to prepare nanocrystals free from the extrinsic effects. In this Chapter we prepared Si nanocrystals fabricated by a gas break–down method. The samples are expected to be free from the extrinsic effects. In Si nanocrystals, the $q=0$ selection rule is relaxed and we must consider phonons in the region of $q\neq0$. The LO and TO phonons are not degenerate at the region of $q\neq0$. Hence two of the dispersion curves were considered, although they were not considered before. Moreover, only the average size of nanocrystals has been previously taken account to discuss the Raman spectra, however it is necessary to consider the size distribution for the precise understanding of the confinement effect. In this study we considered the size distributions obtained through TEM images to analyze the Raman spectra.

In Chapter VIII, we conclude this thesis.

References

[1] A. Jayaraman and A. K. Ramdas, Phys. Today **41** (8), 56 (1988).

[2] *Light Scattering in Solids I*, edited by M. Cardona, (Springer, Berlin, 1975).

[3] *Light Scattering in Solids II*, edited by M. Cardona and G. Güntherodt, (Springer, Berlin, 1982).

[4] *Light Scattering in Solids III*, edited by M. Cardona and G. Güntherodt, (Springer, Berlin, 1982).

[5] *Light Scattering in Solids IV*, edited by M. Cardona and G. Güntherodt, (Springer, Berlin, 1984).

[6] *Light Scattering in Solids V*, edited by M. Cardona and G. Güntherodt, (Springer, Berlin, 1989).

[7] *Light Scattering in Solids VI*, edited by M. Cardona and G. Güntherodt, (Springer, Berlin, 1991).

[8] M. A. Haase, J. Qiu, J. M. DePuydt, and H. Cheng, Appl. Phys. Lett. **59**, 1272 (1991).

[9] Y. Yamada, Y. Masumoto, J. T. Mullins, and T. Taguchi, Appl. Phys. Lett. **61**, 2190 (1992).

[10] T. P. Pearsall, J. Bevk, L. C. Feldman, J. M. Bonar, J. P. Mannaerts, and A. Ourmazd, Phys. Rev. Lett. **58**, 729 (1987).

[11] R. Zachai, K. Eberl, G. Abstreiter, E. Kasper, and H. Kibbel, Phys. Rev. Lett. **64**, 1055 (1990).

[12] A. G. Cullis and L. T. Canham, Nature **353**, 335 (1991).

[13] H. Takagi, H. Ogawa, Y. Yamazaki, A. Ishizaki, and T. Nakagiri, Appl. Phys. Lett. **56**, 2379 (1990).

[14] Y. Kanemitsu, H. Uto, Y. Masumoto, and Y. Maeda, Appl. Phys. Lett. **61**, 2187 (1992).

[15] C. G. Van de Walle and R. M. Martin, Phys. Rev. B **35**, 8154 (1987).

[16] C. G. Van de Walle, Phys. Rev. B **39**, 1871 (1989).

[17] S. Vepřek, Z. Iqbal, H. R. Oswald, and A. P. Webb, J. Phys. C **14**, 295 (1981).

[18] H. Richter, Z. P. Wang, and L. Ley, Solid State Commun **39**, 625 (1981).

[19] Z. Iqbal and S. Vepřek, J. Phys. C **15**, 377 (1982).

[20] I. H. Campbell and P. M. Fauchet, Solid State Commun. **58**, 739 (1986).

[21] M. Fujii, S. Hayashi, and K. Yamamoto, Jpn. J. Appl. Phys. **30**, 687 (1991).

[22] A. Tanaka, S. Onari, and T. Arai, Phys. Rev. B **45**, 6587 (1992).

[23] H. Lamb, Proc. London Math. Soc. **13**, 187 (1882).

[24] B. Champagnon, B. Andrianasolo, and E. Duval, J. Chem. Phys. **94**, 5237 (1991).

[25] M. Fujii, T. Nagareda, S. Hayashi, and K. Yamamoto, Phys. Rev. B **44**, 6243 (1991).

[26] E. Duval, Phys. Rev. B **46**, 5795 (1992).

[27] S. Hayashi and H. Kanamori, Phys. Rev. B **26**, 7079 (1982).

[28] H. Oniyama, S. Yamaga, and A. Yoshikawa, Jpn. J. Appl. Phys. **28**, L2137 (1989).

[29] J. B. Hopkins, L. A. Farrow, and G. J. Fisanick, Appl. Phys. Lett. **44**, 535 (1984).

[30] J. B. Hopkins and L. A. Farrow, J. Appl. Phys. **59**, 1103 (1986).

[31] S. Nakashima, K. Mizoguchi, Y. Inoue, M. Miyauchi, A. Mitsuishi, T. Nishimura, and Y. Akasaka, Jpn. J. Appl. Phys. **25**, L222 (1986).

[32] G. Scamarcio, M. Lugará, and D. Manno, Phys. Rev. B **45**, 13792 (1992).

CHAPTER II

THEORY OF RAMAN SCATTERING

We consider the scattering of photons by phonons. When a monochromatic light of frequency ω_i excites the crystal, the scattered radiation consists of a very strong line at the frequency ω_i, as well as of a series of much weaker lines with frequencies $\omega_i \pm \omega_\mu$, where ω_μ are phonon frequencies. The strong line centered at ω_i is due to elastic scattering of photons and is known as Rayleigh scattering. The series of weak lines at $\omega_i \pm \omega_\mu$ originate from inelastic scattering of photons by phonons and are called Raman scattering.

The chapter start with a discussion of the theoretical treatment of Raman effect on the basis of the radiation emitted by an oscillating dipole (Sect. 2.1).[1,2] We then give properties of phonon in low–dimensional structures, especially strained–layer superlattices (SLSs) and nanocrystals. In Sect. 2.2 we discuss the properties of acoustic phonons and optical phonons in SLSs. Finally, the phonon confinement effects in nanocrystals are discussed on the basis of a spatial correlation (SC) model in Sect. 2.3.

2.1 Raman Scattering from Lattice Vibrations

Let the electric field of the incident light $\mathbf{E}_i$ is given by

$$E_i = e_i E_{0i} \exp[j(\omega_i t - k_i \cdot r)], \tag{2.1}$$

where $\mathbf{e}_i$ and $\mathbf{k}_i$ are the unit vector of polarization and the wavevector, respectively. The dipole moment $\mathbf{M}$ is induced by the electric field and is given by

$$\boldsymbol{M}=[\alpha]\boldsymbol{E}_i. \tag{2.2}$$

Here $[\alpha]$ is the electronic polarizability tensor. The electronic polarizability depends on the electric charge distribution in the crystal. If the atomic configuration changes during the lattice vibration, charge distribution and hence $[\alpha]$ will be modified. Therefore, $[\alpha]$ will change linearly with the phonon normal coordinate u_μ. Expanding $[\alpha]$ in a Taylor's series, we obtain

$$[\alpha]=[\alpha]_0+\sum_\mu\left(\frac{\partial[\alpha]}{\partial u_\mu}\right)_0 u_\mu+\frac{1}{2}\sum_{\mu,\mu'}\left(\frac{\partial^2[\alpha]}{\partial u_\mu \partial u_{\mu'}}\right)_0 u_\mu u_{\mu'}+\cdots. \tag{2.3}$$

If the lattices vibrate with the frequencies ω_μ and wavevectors q_μ we have

$$u_\mu=A_\mu \exp[\pm j(\omega_\mu t-\boldsymbol{q}_\mu\cdot\boldsymbol{r})]. \tag{2.4}$$

Substituting Eqs. (2.3) and (2.4) into Eq. (2.2) gives

$$\begin{aligned}\boldsymbol{M}=&[\alpha]_0\boldsymbol{e}_i E_{0i}\exp[j(\omega_i t-\boldsymbol{k}_i\cdot\boldsymbol{r})]\\ &+\sum_\mu\left(\frac{\partial[\alpha]}{\partial u_\mu}\right)_0 \boldsymbol{e}_i A_\mu E_{0i}\exp\{j[(\omega_i\pm\omega_\mu)t-(\boldsymbol{k}_i\pm\boldsymbol{q}_\mu)\cdot\boldsymbol{r}]\}\\ &+\frac{1}{2}\sum_{\mu,\mu'}\left(\frac{\partial^2[\alpha]}{\partial u_\mu\partial u_{\mu'}}\right)_0 \boldsymbol{e}_i A_\mu A_{\mu'} E_{0i}\exp\{j[(\omega_i\pm\omega_\mu\pm\omega_{\mu'})t+(\boldsymbol{k}_i\pm\boldsymbol{q}_\mu\pm\boldsymbol{q}_{\mu'})\cdot\boldsymbol{r}]\}+\cdots.\end{aligned} \tag{2.5}$$

Equation (2.5) shows that the induced dipole moment **M** vibrates not only with the frequency ω_i of the incident light, but also with the frequency $\omega_i\pm\omega_\mu$ and $\omega_i\pm\omega_\mu\pm\omega_{\mu'}$. The first term in Eq. (2.5) is responsible for Rayleigh scattering, while the second and the third terms give rise to first- and second-order Raman scattering.

This oscillating dipole radiates the electromagnetic wave, i. e., dipole moment radiation. The radiated electric and magnetic field, $\mathbf{E}_s$ and $\mathbf{H}_s$ can be given by

$$\begin{aligned} &\boldsymbol{E}_s=\boldsymbol{n}\times(\boldsymbol{n}\times\ddot{\boldsymbol{M}})/c^2R, \\ &\boldsymbol{H}_s=(\ddot{\boldsymbol{M}}\times\boldsymbol{n})/c^2R, \end{aligned} \tag{2.6}$$

where **n** is the unit vector of the radiation. When we consider the term of the first-order Raman scattering in Eq. (2.5), we obtain

$$\boldsymbol{E}_s=-\sum_{\mu}\frac{(\omega_i\pm\omega_\mu)^2}{c^2R}\left\{\boldsymbol{n}\times\left[\boldsymbol{n}\times\left(\frac{\partial[\alpha]}{\partial u_\mu}\right)_0\cdot\boldsymbol{e}_i\right]\right\}A_\mu E_{0i}\exp\{j[(\omega_i\pm\omega_\mu)t-(\boldsymbol{k}_i\pm\boldsymbol{q}_\mu)\cdot\boldsymbol{r}]\}. \tag{2.7}$$

The electric field scattered by the μ-mode lattice vibration, $\mathbf{E}_s^{\mu}$, can be expressed by

$$\boldsymbol{E}_s^{\mu}=\boldsymbol{e}_s E_{0s}\exp[j(\omega_s t-\boldsymbol{k}_s\cdot\boldsymbol{r})], \tag{2.8}$$

where $\mathbf{e}_s$, ω_s, and $\mathbf{k}_s$ are the unit vector of polarization, the frequency, and the wavevector of the radiated electric field. Comparing Eq. (2.8) with Eq. (2.7), we obtain

$$\begin{aligned} &\omega_s=\omega_i\pm\omega_\mu, \\ &\boldsymbol{k}_s=\boldsymbol{k}_i\pm\boldsymbol{q}_\mu. \end{aligned} \tag{2.9}$$

Equation (2.9) shows the conservation of energy and momentum. The plus and minus signs correspond to the anti-Stokes and Stokes processes, respectively. For typical Raman scattering experiments, we use in- or near-visible light and the magnitude of the scattered wavevector $|\mathbf{k}_s|$ is less than 10^6 cm^{-1}. This implies that for the first-order Raman scattering processes, the accessible range of $|\mathbf{q}_\mu|$ is small compared to a reciprocal lattice wavevector ($\sim 10^8$ cm^{-1}). Therefore the phonons with $q \cong 0$ can be observed in the first-order Raman scattering measurements.

The energy flux of the scattered light is given by

$$\boldsymbol{S}=\frac{c}{4\pi}(\boldsymbol{E}_s\times\boldsymbol{H}_s)=\frac{c}{4\pi}|\boldsymbol{E}_s|^2\boldsymbol{n}, \tag{2.10}$$

where S is a Poynting vector. The magnitude of the Poynting vector S is proportional to the production of $\mathbf{E}_s^{\mu}$ and $\ddot{\mathbf{M}}$, and Eq. (2.10) becomes

$$S_\mu = |E_s^\mu \cdot \ddot{M}|^2 \frac{n}{4\pi R^2 c^3}. \tag{2.11}$$

Using the second derivative of Eq. (2.5) with respect to the time and Eq. (2.8), we obtain

$$S_\mu = \frac{(\omega_i \pm \omega_\mu)^4 n}{4\pi R^2 c^3} A_\mu^2 E_{0i}^2 E_{0s}^2 \left| e_s \cdot \left(\frac{\partial[\alpha]}{\partial u_\mu} \right)_o \cdot e_i \right|^2. \tag{2.12}$$

Equation (2.12) shows the relation of the polarization between the incident and scattered light. The Raman processes can be allowed when the polarizations satisfy the following selection rule:

$$\left| e_s \cdot \left(\frac{\partial[\alpha]}{\partial u_\mu} \right)_o \cdot e_i \right| \neq 0. \tag{2.13}$$

The terms of $(\partial[\alpha]/\partial u_\mu)_0$ is called a Raman tensor. The Raman tensor of the allowed scattering have been tabulated for all crystal classes by Loudon.[3] By choosing different polarization configuration it is possible to observe the different components of the Raman tensor. This information is of considerable importance for the assignment of the vibration symmetry of the observed phonons.

2.2 Raman Scattering in Strained-Layer Superlattices

In this section, the superlattices made out of diamond- or zincblende-type bulk constituents are discussed. Let us assume that the two constituents (materials 1 and 2) have the layer thicknesses d_1 and d_2. The superlattices have a new period along growth direction z being $d=d_1+d_2$. Because of the enhancement of the period along the growth direction z, the Brillouin zone (BZ) must be folded into a smaller mini-BZ. After zone-folding, new modes appear in the mini–BZ at q=0. These modes can now be Raman active and are called zone-folded modes.[4]

For acoustic phonons, the dispersion relations are linear and can be observed a few peaks of folded modes. The theoretical treatment of the acoustic zone–folded modes are discussed in Sect. 2.2.1.

Whereas, the dispersion curves of bulk optical branches are usually flat and the group velocities are small. Hence, the optical phonon becomes a standing wave and is confined in the alternating layers.[5] Most of the crystals of zincblende structure has the maximum LO phonon energy located at the point of q=0 in the reciprocal lattice space. Hence the higher-order optical phonon modes are located at lower energy side. When the period d is longer than 10 monolayers, the difference of the peak position of the higher order modes is very small (less than 1 cm^{-1}) and can not be distinguished because of the wider peak width.[5] Hence, the spectral shape of the optical modes have a tail in lower energy side in the large period superlattices.

Another topic concerning optical phonons is a strain effect. Most of the superlattices have inherent stress at the heterojunction interface due to the lattice mismatch. For example, the lattice mismatch in ZnSe–ZnS superlattices is about 4.5%. They become strained–layer superlattices (SLSs) within the critical thicknesses.[6] There exists a stress lying in the plane parallel to the interface. In this sense they have quasi–two–dimensional structures. In Sect. 2.2.2 we concentrate the stress effect on Raman scattering spectrum.

2.2.1 Zone Folding of Acoustic Modes

In acoustic region, the zone–folded modes of LA phonons are Raman–active. The dispersion curves of the folded LA modes were calculated on the basis of the layered elastic continuum model by Rytov.[7] The dispersion is written by

$$\cos(qd)=\cos\left(\frac{\omega d_1}{v_1}\right)\cos\left(\frac{\omega d_2}{v_2}\right)-\frac{1+\kappa^2}{2\kappa}\sin\left(\frac{\omega d_1}{v_1}\right)\sin\left(\frac{\omega d_2}{v_2}\right), \tag{2.14}$$

where ω and q are the phonon frequency and the superlattice wavevector, v_1 and v_2 are the sound velocities of materials 1 and 2, and d is the period of the superlattices. The coefficient κ is defined by

$$\kappa \equiv v_1 \rho_1 / v_2 \rho_2, \tag{2.15}$$

where ρ_1 and ρ_2 are the corresponding densities.

It can be assumed that the q conservation rule leads to q=0 in a bulk material (Sect. 2.1). However it is not correct in superlattices because the incident wavevector $\mathbf{k}_i$ is not so small compared to the wavevector of the mini-BZ. Therefore the exact formula of Eq. (2.9) should be adopted. Because of $q \neq 0$, the cross points of q and the dispersion curve given by Eq. (2.14) become doublet. In the small energy region, the approximate dispersion relation for the *m*th order doublet is

$$\omega_m = |2m\pi/d \pm q| v_{sl}, \tag{2.16}$$

where v_{sl} is sound velocity of superlattices defined by

$$d/v_{sl} = d_1/v_1 + d_2/v_2. \tag{2.17}$$

The intensity of Raman scattering from the folded LA modes can be theoretically calculated by a photoelastic model.[8,9] The photoelastic model has been used previously to predict the intensity of the folded modes[10] and to characterize the periodicity and roughness of the interface[11] in GaAs-$Ga_xAl_{1-x}As$ superlattices.

The Raman scattering of folded LA modes originates from the photoelastic effect. The polarizability M(z) can be written as[9]

$$M(z) = P(z)\frac{\partial u(z)}{\partial z}E_i(z). \tag{2.18}$$

Here P(z) is the local value of the photoelastic coefficient, u(z) is the longitudinal displacement, and $E_i(z)$ is the electric field produced by the incident light. It can be assumed that the superlattices have bulk photoelastic coefficients P_1 and P_2. Thus P(z) reflects the structural profile of the superlattices. The quantities P(z) and u(z) can be expanded in Fourier series:

$$\begin{aligned} P(z) &= \sum_n Q_n e^{jnGz}, \\ u(z) &= e^{-jqz}\sum_n u_{n,-q} e^{jnGz}, \\ E_i(z) &= E_i e^{jk_iz}, \end{aligned} \tag{2.19}$$

where G=2π/d. Substituting Eq. (2.19) into Eq. (2.18), we obtain

$$M_{k_i-q} = \sum_n Q_{-n} u_{n,-q} j(nG-q)E_i. \tag{2.20}$$

The *m*th term in this sum describes Raman scattering of folded LA phonons has intensity at ω_m and,

$$\begin{aligned} I_m &\propto \omega_m(n_m+1)E_i^2 |Q_m u_{m,-q}(mG-q)|^2 \\ &\propto \omega_m(n_m+1)|Q_m|^2, \end{aligned} \tag{2.21}$$

where n_m is the Bose factor. Equation (2.21) indicates that the relative intensity of the folded modes can be calculated, when the structural profile of the superlattices P(z) is known.

2.2.2 Strain Effect in Heterojunctions

As mentioned above, there exists a biaxial stress in the heterojunctions. In this section, it is proposed that this stress causes a spitting of optical phonon modes. Let the growth direction of the heterojunctions is parallel to <001> axis. When a_1 and a_2 are defined as the unstrained lattice constants of bulk materials 1 and 2, the lattice constant of the strained layers in the plane parallel to the interface ($a_{//}$) is given by the following equation:[12]

$$a_{\parallel}=a_2\left(1+\frac{fG_1d_1}{G_1d_1+G_2d_2}\right), \tag{2.22}$$

where f is the lattice mismatch defined by the equation, $f=(a_1-a_2)/a_2$, G_1 and G_2 are shear moduli.

The components of strain-tensor parallel to the interface plane are given by

$$\varepsilon_{xx}=\varepsilon_{yy}=(a_{\parallel}-a)/a=(S_{11}+S_{12})X, \tag{2.23}$$

where S_{11} and S_{12} are elastic compliance constants and X is the strength of the stress. Following Cerdeira *et al.*[13], we can obtain two types of the energy deviations from the energy of bulk modes (ω_0) under biaxial stress in the (001) plane:

$$\begin{aligned}\Delta\Omega_s&=[pS_{12}+q(S_{11}+S_{12})]X/\omega_0,\\ \Delta\Omega_d&=[p(S_{11}+S_{12})+q(S_{11}+3S_{12})]X/2\omega_0,\end{aligned} \tag{2.24}$$

where p and q are parameters proportional to the changes of the spring constant induced by the strain (see Appendix). In Eq. (2.24), $\Delta\Omega_s$ indicates the shift of the singlet-type mode vibrating parallel to the <001> axis, while $\Delta\Omega_d$ indicates the shift of doublet-type modes vibrating perpendicular to the <001> axis. This splitting occurs because the biaxial stress makes the sample quasi-two-dimensional.

2.3 Raman Scattering in Nanocrystals

In nanocrystals, some interesting facts have been observed by means of Raman scattering, such as confinement of optical phonons,[14-19] two types of new acoustic modes,[20-23] and a surface mode.[24]

When the crystal size decreases to be an order of nanometer, the optical phonon modes are confined in the nanocrystal and the q=0 selection rule is relaxed. The confinement effect in the nanocrystal is larger than in the superlattices. This is because the vibrations in the nanocrystal are confined three–dimensionally, whereas confined only in one direction along z in superlattices. The peak position shifts lower energy side and the spectral shape becomes asymmetric due to the confinement effect. A quantitative model calculation for nanocrystals which takes into account of the phonon confinement effect was developed by Richter *et al.*[15] Later Campbell and Fauchet[17] expand this model calculation and obtained the relationship between the nanocrystal size, the peak shift, and the spectral shape. This model is often called spatial correlation (SC) model.

In acoustic region, no folded modes were observed because there is no long range periodicity in nanocrystals. The acoustic vibration modes of a spherical particles were, at first, studied by Lamb.[20] He suggested the existence of two types of modes, that is a spheroidal and a torsional modes. However good–quality data has not been reported so far and this problem is now under investigation.

Another topic of Raman scattering in nanocrystals is the surface phonon. Hayashi *et al.*[24] studied the surface phonon mode in GaP nanocrystals and observed that the surface modes show three characteristic features which were predicted theoretically.

In this Section, we concentrate the confinement effect of optical phonons following the SC model.[15,17] The wave function of a phonon with wave vector $\mathbf{q}_0$ in an infinite crystal is

$$\phi(q_0,t)=u(q_0,r)\exp(jk_0\cdot r-j\omega_0 t)\exp(-t/\tau_0), \qquad (2.25)$$

where $\mathbf{u}(\mathbf{q}_0,\mathbf{r})$ is a Bloch function and τ_0 is a phonon lifetime. The nanocrystal is assumed to be spherical with a diameter L. The phonon is confined in the volume of the nanocrystal. In order to impose this confinement effect, we replace ϕ by a new function ψ:

$$\begin{aligned}\psi(q_0,r)&=\gamma\exp\left[-\frac{r^2/2}{(L/2)^2}\right]\phi(q_0,r)\\&=\gamma\exp\left(-\frac{2r^2}{L^2}+jk_0\cdot r\right)\exp(-j\omega_0 t-t/\tau_0)u(q_o,r).\end{aligned}\tag{2.26}$$

Equation (2.26) means that ψ is localized to $|r|<L/2$ in the form of a Gauss distribution. The function ψ can be expanded in a Fourier series:

$$\psi(q,\omega)=\frac{\gamma}{j}(\pi L^2/2)^{3/2}\exp\left(-\frac{q^2L^2}{8}\right)\frac{1}{1/\tau_0-j(\omega-\omega_0)}.\tag{2.27}$$

Here $\omega(q)$ is the phonon dispersion curve. The amplitude of this wave function is given by

$$|\psi(q,\omega)|^2=\gamma^2(\pi L^2/2)^3\exp\left(-\frac{q^2L^2}{4}\right)\frac{1}{(\omega-\omega_0)^2+(1/\tau_0)^2}.\tag{2.28}$$

The term of $\exp(-q^2L^2/4)$ indicates the relaxation of the $q=0$ selection rule. The Raman intensity is proportional to the integral of Eq. (2.28) in the region of BZ:

$$I(\omega,L)\propto\int_0^{2\pi/a}\exp\left(-\frac{q^2L^2}{4}\right)\frac{1}{(\omega(q)-\omega_0)^2+(1/\tau_0)^2}dq^3.\tag{2.29}$$

In order to calculate the theoretical Raman spectrum, we must integrate Eq. (2.29) over entire BZ. However, the integration is difficult because of the anisotropy of the phonon dispersion relations. As far as the nanocrystal size remains large enough, significant contribution to the integral comes from a relatively small region at the center of the BZ and the anisotropy in that region is not so large. Therefore we assume that the BZ is spherical and the phonon dispersion curves are isotropic.

Richter *et al.*[15] assumed that the phonon amplitude at the boundary of the nanocrystal decays e^{-1}. However this assumption does not explain the experimental results quantitatively. Later Campbell and Fauchet[17] determined the boundary condition to fit the experimental data and reported that the data agree well when the amplitude at the boundary is $\exp(-4\pi^2)$. In Chap. VII, we will use the SC model with the boundary condition determined by Campbell and Fauchet.

References

[1] P. Brüech, *Phonons:Theory and Experiments II*, (Springer, Berlin, 1986), p. 65.

[2] K. Mizoguchi, Ph. D. Thesis, Osaka University, 1988.

[3] R. Loudon, Adv. Phys. **13**, 423 (1964); **14**, 621 (E) (1965).

[4] See, for example, *Light Scattering in Solids V*, edited by M. Cardona and G. Güntherodt, (Springer, Berlin, 1989).

[5] M. Nakayama, K. Kubota, T. Kanata, H. Kato, S. Chika, and N. Sano, Jpn. J. Appl. Phys. **24**, 1331 (1985).

[6] G. C. Osbourn, IEEE J. Quantum Electron. **QE–22**, 1677 (1986).

[7] S. M. Rytov, Akust. Zh. **2**, 71 (1956) [Sov. Phys. Acoust. **2**, 68 (1956)].

[8] C. Colvard, T. A. Gant, M. V. Klein, R. Merlin, R. Fischer, H. Morkoç, and A. C. Gossard, Phys. Rev. B **31**, 2080 (1985).

[9] B. Jusserand, D. Paquet, F. Mollot, F. Alexandre, and G. Le Roux, Phys. Rev. B **35**, 2808 (1987).

[10] M. V. Klein, C. Colvard, R. Fischer, and H. Morkoç, J. Phys. (Paris) Colloq. C **5**, 131 (1984).

[11] S. K. Hark, B. A. Weinstein, and R. D. Burnham, J. Appl. Phys. **62**, 1112 (1987).

[12] J. W. Matthews and A. E. Blakeslee, J. Cryst. Growth **32**, 265 (1976).

[13] F. Cerdeira, C. J. Buchenauer, F. H. Pollak, and M. Cardona, Phys. Rev. B **5**, 580 (1972).

[14] S. Vepřek, Z. Iqbal, H. R. Oswald, and A. P. Webb, J. Phys. C **14**, 295 (1981).

[15] H. Richter, Z. P. Wang, and L. Ley, Solid State Commum **39**, 625 (1981).

[16] Z. Iqbal and S. Vepřek, J. Phys. C **15**, 377 (1982).

[17] I. H. Campbell and P. M. Fauchet, Solid State Commun. **58**, 739 (1986).

[18] M. Fujii, S. Hayashi, and K. Yamamoto, Jpn. J. Appl. Phys. **30**, 687 (1991).

[19] A. Tanaka, S. Onari, and T. Arai, Phys. Rev. B **45**, 6587 (1992).

[20] H. Lamb, Proc. London Math. Soc. **13**, 187 (1882).

[21] B. Champagnon, B. Andrianasolo, and E. Duval, J. Chem. Phys. **94**, 5237 (1991).

[22] M. Fujii, T. Nagareda, S. Hayashi, and K. Yamamoto, Phys. Rev. B **44**, 6243 (1991).

[23] E. Duval, Phys. Rev. B **46**, 5795 (1992).

[24] S. Hayashi and H. Kanamori, Phys. Rev. B **26**, 7079 (1982).

CHAPTER III

EXPERIMENTAL

Two types of Raman scattering measurement systems were used in this study, that is macro– and micro–Raman scattering measurement systems. Figure 3.1 shows the apparatus of the macro–Raman measurement system. Some of the lasing lines of an Ar ion laser were used to excite the sample. The monochromatic laser beam passes through the laser filter monochromator which rejects the plasma lines. The laser beam then focused by the lens onto the sample. The spot size of the laser beam is about 100 μm. The scattered light from the sample is focused by the camera lens onto the entrance slit of the 85 cm double monochromator (Spex; 1403). For a polarization experiment, an analyzer was used *in front* of the slit and after that polarized light passes a Babinet compensator to scramble the polarization. The analyzed light is focused onto the photomultiplier (RCA; C31034) and the number of output electric pulses are amplified and counted by the multichannel analyzer (Tracor Northern; TN–1710). The output of the signal are acquired by the personal computer (NEC; PC–9801). The personal computer also controls the sweep of the double monochromator and can get the spectrum.

The apparatus of the micro–Raman scattering measurement system is shown in Fig. 3.2. It shows a Raman microprobe measurement system (Japan Spectroscopic Co., Ltd.; NR–1000). The most different point from the macro–Raman measurement system is that the laser is focused by a microscope. In this system spot size on the sample surface can be reduced to ~1 μm. Therefore the Raman signal from the region of ~1 μmϕ can be measured. The scattered light are analyzed by a 25 cm filter double monochromator and a 1 m monochromator. The detector used here is a photodiode array (Tracor Northern; TN−6122) with the optical multichannel analyzer (Seki Technotoron; SK−297).

In order to estimate the spot size of the laser beam at the sample surface, we scan the laser beam on the edge of the bulk Si and measured the intensity of the reflected light. The schematic measurement apparatus is shown in the inset of Fig. 3.3. Figure 3.3 shows the reflected intensity as a function of the position of the laser. The solid line shows the fitted curve where the beam profile is assumed to be a Gaussian shape. The spot size, the fitting parameter, was estimated to be 1.3 μm in diameter.

When we use the micro−Raman measurement, it takes only a few minutes to get a Raman spectrum and we can obtain the information of small sample region. However, there are two demerits in this measurement system. The system has exactly backscattering configuration and the laser reflected by the sample is also enters into the monochromator. Therefore, intense stray line goes through the monochromator and this makes it difficult to measure a low frequency region (ω<200 cm^{-1}). This is the first point of the demerits. The second is that the spectral range measured in one scan is limited by the width of the photodiode array and is about 500 cm^{-1}. Therefore, when the low frequency region or wide spectral range is needed, the macro−Raman measurement should be used.

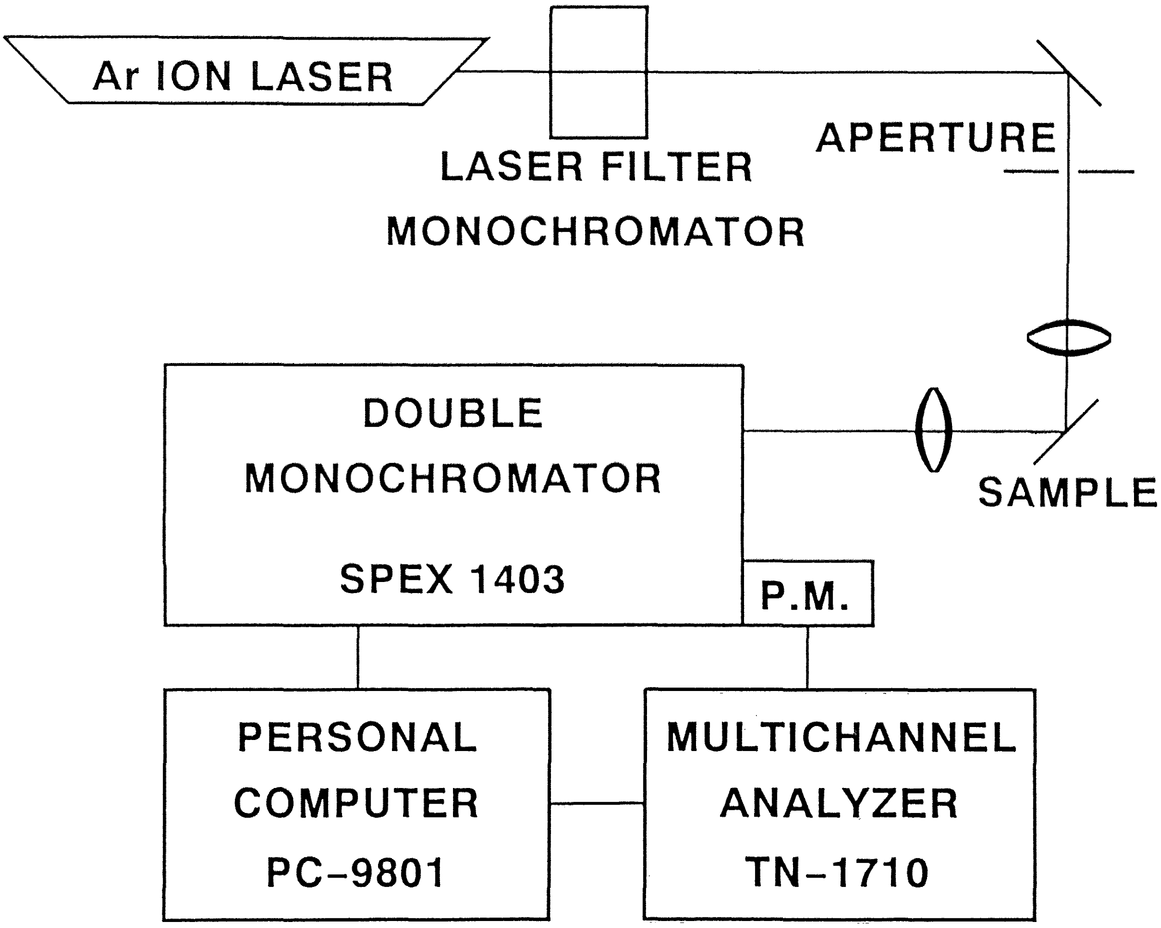

Fig. 3.1. Apparatus of macro–Raman scattering measurement system.

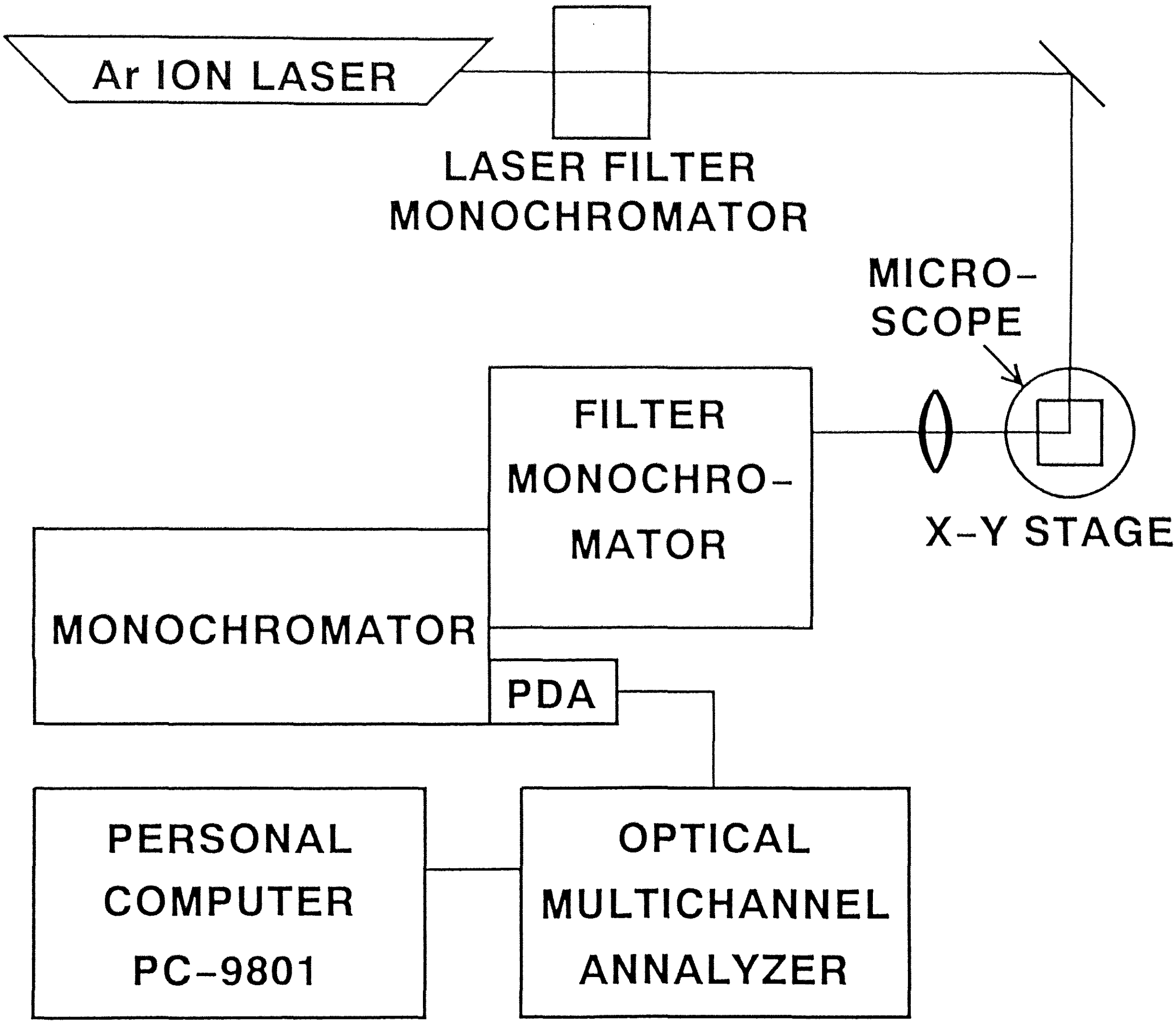

Fig. 3.2. Apparatus of micro–Raman scattering measurement system.

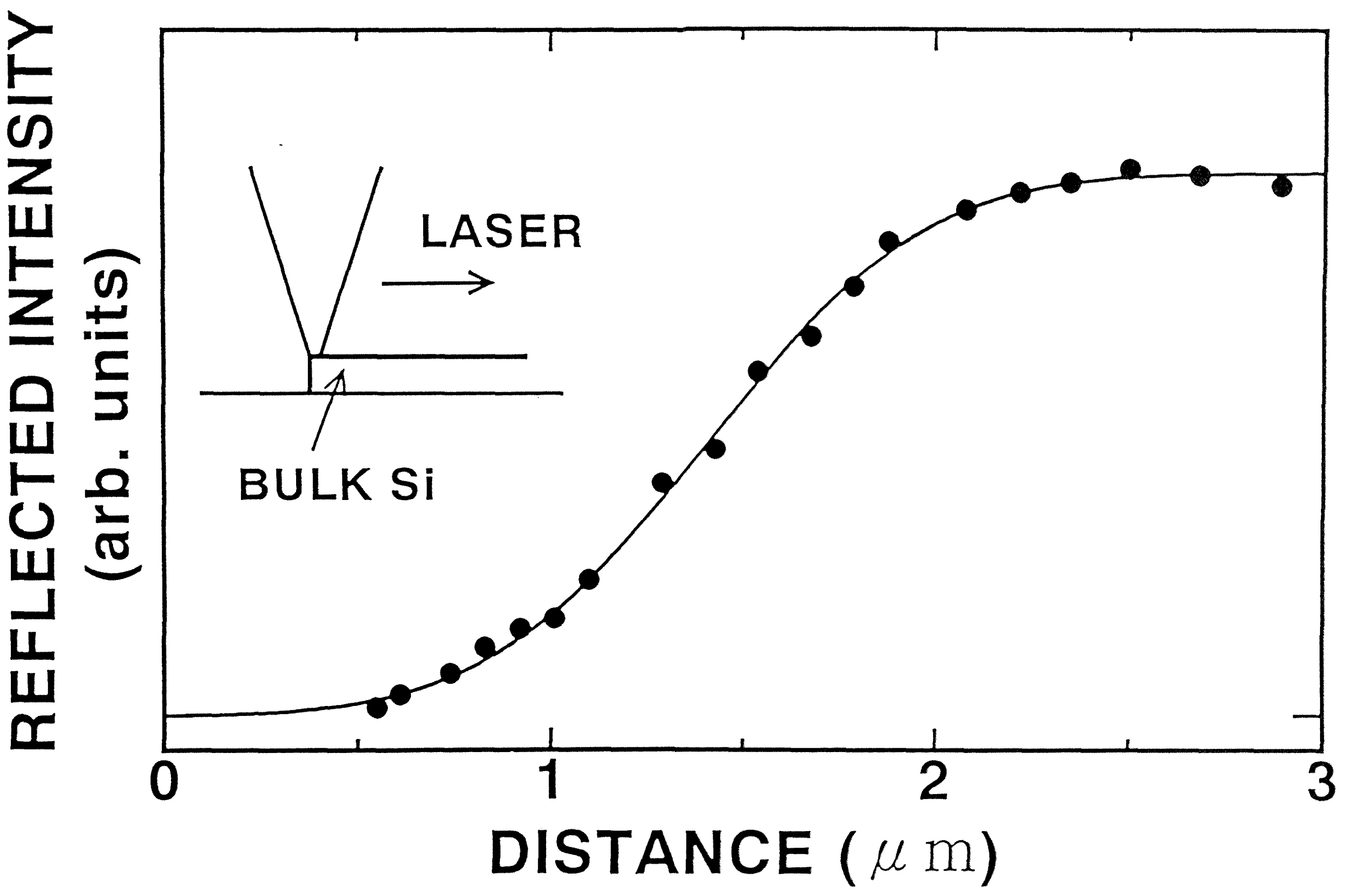

Fig. 3.3. Reflected laser intensity when the laser beam crosses an edge of a Si wafer. The solid line shows the fitted curve where the beam profile is assumed to be a Gaussian shape. The spot size was estimated to be 1.3 μm in diameter.

CHAPTER IV

HIGHER-ORDER ZONE-FOLDED ACOUSTIC MODES

Most of the II–VI semiconductor spuperlattices have a biaxial stress at the heterojunction interface due to the lattice mismatch. For example, stress-induced peak shifts of optical phonons were observed in strained-layer superlattices (SLSs).[1-5] The spectra of zone-folded acoustic phonons were broad and only the first or second order were previously observed.[6,7] One speculates that the lattice mismatch makes it difficult to establish high-quality epitaxial layers and to observe zone-folded modes.

The stress comes from two types of lattice mismatch which exists between SLSs and a substrate, and between the alternate layers in the SLSs. In this study we were able to observe higher order doublet phonon modes, up to the 5th order, in ZnSe–ZnS SLSs whose average lattice constant is equal to that of a GaAs substrate.[8] We tried to answer two questions here. One is why such higher order folded modes were observed. The other is whether or not the stress matters to the zone folding of phonon modes. A model calculation based on the transmission electron microscopy (TEM) data was used to consider these problems.

4.1 Experimental Results

A sample used in this work was ZnSe–ZnS SLSs grown by metalorganic molecular beam epitaxy (MOMBE) on a (100) GaAs substrate.[8] The designed thickness of ZnSe and ZnS layers were 200 and 10 Å, respectively. The average lattice constant of the SLSs was equal to the GaAs substrate in order to reduce the stress between the SLSs and the substrate.

Figure 4.1 shows polarization dependence of Raman spectra. The excitation laser wavelength was 4765 Å and the macro-Raman measurement system was used in quasi-backscattering configuration on (100) plane. The sample was kept in vacuum to avoid scattering from the air. Several peaks were observed assigned to be the zone-folded longitudinal acoustic (LA) modes. Fig. 4.1 shows all the zone-folded modes are allowed in $z(x,x)\bar{z}$ configuration and are forbidden in $z(x,y)\bar{z}$ configuration, where x and y denote the polarization of the incident and scattered light (x//<100>, y//<010>). However, group theoretical analysis predicts that the lower energy mode of the doublet is allowed only in $z(x,x)\bar{z}$ configuration whereas the higher energy mode is allowed only in $z(x,y)\bar{z}$ configuration. The same results were obtained in GaAs-GaAlAs superlattices.[9] Jusserand *et al.*[9] attributed the breaking of the selection rules to the fact that the non-zone-center phonons display other symmetry.

Figure 4.2(a) shows the spectrum where the background was subtracted from the spectrum of Fig. 4.1. The background is probably originated from Rayleigh scattering and single particle excitations.[10] Figure 4.2(a) shows zone-folded doublet modes up to the 5th order. To our knowledge, it is the first observation of such higher order modes in II-VI SLSs.

4.2 Discussion

The peak positions of the folded-modes were calculated using the phonon dispersion curve given by Eq. (2.14). The inset of the Fig. 4.2(a) shows the dispersion curve. The parameters used in the calculation are listed in Table 4.1. The sound velocities used in this calculation were stress-free values in bulk crystals. The solid circles in the inset are observed peak frequencies of the folded modes which were estimated from the peak positions of the

Stokes and anti–Stokes zone–folded spectra. When the thicknesses of ZnSe and ZnS, d_1 and d_2, are designed values, 200 Å and 10 Å, the calculated peak energies do not agree well with the observed ones. The period, d, was estimated to be 205 Å from the x–ray diffraction measurement,[8] though the constituting layer thicknesses, d_1 and d_2, were not obtained exactly. Therefore, we fixed the period, d, to be 205 Å, and varied the layer thicknesses, d_1 and d_2, to fit the all of the observed frequencies of the zone–folded modes. The fitted values of d_1 and d_2 were 198 Å and 7 Å, respectively. These values were used to calculate the dispersion shown in the inset of Fig. 4.2(a). The calculation fits the experimental data satisfactorily.

So far, zone–folded modes were observed in ZnTe–ZnSe[6,11] and InAs–AlAs[7] SLSs. It was suggested that the observed peak energies of the folded modes do not completely agree with the calculated ones. This discrepancy was believed to be originated from the strain between the alternate layers. Recio *et al.*[7] considered the effect of the strain on the sound velocities deduced from the stress–induced peak shifts of LO–Raman modes and Grüneisen constants. We tried to include the stress effect on the sound velocities using their method. However all the estimated peak energies were larger than the observed ones by $\sim 0.2\ \mathrm{cm}^{-1}$. The calculation does not fit the experimental data better than the stress–free calculation. Furthermore, it was found that the changing of the thicknesses by a few angstrom induces the peak shift of the folded modes more than the stress.

Figures 4.3(a) and 4.3(b) show low– and high–resolution transmission electron microscopy (TEM) images of the sample, respectively. Figure 4.3(a) shows good periodicity of each layer. However a large fluctuation exists near the interface as shown in Fig. 4.3(b). Figure 4.3(c) shows the histogram of the lattice points of ZnS. We obtained the each data in the histogram by counting the lattice points of ZnS along the straight arrays of lattice points parallel to the interface plane. The full width at half maximum (FWHM) of the histogram is about 4 layers and it is a little larger than the fitted value for the thickness of the ZnS layer, 7 Å. The position at the center of the ZnS layers is fluctuated. Therefore the FWHM of the histogram is larger than the thickness of the ZnS layer.

In Sect. 2.2.1, we have shown that the intensity of Raman scattering from the folded LA modes can be theoretically calculated by a photoelastic model, where the superlattices have bulk photoelastic coefficients P_1 and P_2. According to this model, the modulation of photoelastic coefficient, P(z), along the growth direction z reflects the modulation in the structure of the SLSs. It is noted that we do not need the absolute values of P_1 and P_2, but need only the lineshape of P(z) in order to calculate the intensity of Raman spectrum.

When P(z) is assumed to be a square-wave function, in an ideal case, the *m*th order Fourier component Q_m is given by

$$|Q_m|^2 = \left| \frac{P_2 - P_1}{\pi m} \sin\left(\frac{\pi m d_1}{d} \right) \right|^2 . \tag{4.1}$$

The Fourier power spectrum is shown in Fig. 4.4(a). The higher order Raman intensity can be calculated by using Eq. (2.21) and is shown in Fig. 4.4(b). Figure 4.4(b) shows that the higher order I_m decreases very slowly and the square-wave assumption can not reproduce the experimental spectrum at all.

Then the fluctuation of the periodicity and the interface roughness were considered from the TEM data. The roughness of the interface was directly deduced from the distribution of ZnS layers as shown in Fig.4.3(c). The fluctuation of the periodicity, that is the fluctuation of the ZnSe layer thickness, was deduced from two-dimensional densitometric data of the low-resolution TEM image [Fig. 4.3(a)]. Thus the profile of P(z) was obtained by taking account of the fluctuation of the periodicity and the roughness of the interface. Figure 4.5(a) shows the obtained profile of P(z). The intervals between the peaks, that is the fluctuation of the periodicity, are shown in Fig. 4.5(a). Figure 4.5(b) shows the Fourier power spectrum, $|Q(k)|^2$ where k is the wavenumber defined by $k=2\pi/z$. Several peaks show the *m*th order Fourier components. The roughness of the interface and the fluctuation of the periodicity cause the decrease of the higher order Q_m. The fluctuation of the periodicity also causes the broadening of the higher order Q_m. By using Eq. (2.21) and the Fourier components Q_m, the Raman spectrum of zone-folded modes was calculated as shown in Fig. 4.2(b). The Raman spectrum reproduces the experimental data in the following two essential points: the higher order modes becomes wider and more than 6th order modes reduce their height obviously. In this calculation, we have assumed that the roughness of the each layer interfaces is the same. If the roughness of the each layer interfaces is taken into account, the intensity of the higher order zone-folded modes decreases more and the model calculation reproduces the Raman spectrum more precisely.

4.3 Summary

We have observed higher order (up to the 5th order) zone-folded acoustic modes in ZnSe-ZnS strained-layer superlattices (SLSs). We were able to reproduce the zone-folded spectrum using TEM data and a photoelastic model. The agreement between our calculation and the measurement shows that the Raman spectrum reflects dominantly the periodicity of the superlattices and the roughness of the interface. Furthermore, the stress does not play an important role to the observation of the zone-folded modes.

References

[1] S. Nakashima, Y. Nakakura, H. Fujiyasu, and K. Mochizuki, Appl. Phys. Lett. **48**, 236 (1986).

[2] M. Nakayama, K. Kubota, H. Kato, S. Chika, and N. Sano, Appl. Phys. Lett. **48**, 281 (1986).

[3] L. H. Shon, K. Inoue, K. Murase, H. Fujiyasu, and Y. Yamazaki, Solid State Commun. **62**, 621 (1987).

[4] L. H. Shon, K. Inoue, O. Matsuda, K. Murase, T. Yokogawa, and M. Ogura, Solid State Commun. **67**, 779 (1988).

[5] A. Yamamoto, Y. Yamada, and Y. Masumoto, Appl. Phys. Lett. **58**, 2135 (1991).

[6] Y. H. Wu, H. Yang, A. Ishida, H. Fujiyasu, S. Nakashima, and K. Tahara, Appl. Phys. Lett. **54**, 239 (1989).

[7] M. Recio, G. Armelles, A. Ruiz, A. Mazuelas, and F. Briones, Appl. Phys. Lett. **54**, 804 (1989).

[8] H. Oniyama, S. Yamaga, and A. Yoshikawa, Jpn. J. Appl. Phys. **28**, L2137 (1989).

[9] B. Jusserand, D. Paquet, A. Regreny, and J. Kervarec, Solid State Commun. **48**, 499 (1983).

[10] M. V. Klein, in *Light Scattering in Solids*, edited by M. Cardona, (Springer, Berlin, 1975) p.148.

[11] J. Cui, H. Wang, and F. Gan, J. Crys. Growth **117**, 505 (1992).

Table 4.1. Parameters for ZnSe and ZnS used in the calculation of Rytov model.

	ZnSe	ZnS
d (Å)	198	7
v (10^5 cm/s)[a]	4.054	5.047
ρ (g/cm^3)[a]	5.266	4.086

[a] Landolt–Börnstein, *Numerical Data and Functional Relationships in Science and Technology* (Semiconductors —— Physics of II–VI and I–VII Compounds, Semimagnetic Semiconductors), edited by O. Madelung, M. Schulz, and H. Weiss (Springer, Berlin, 1982), Vol. 17(b), p. 145.

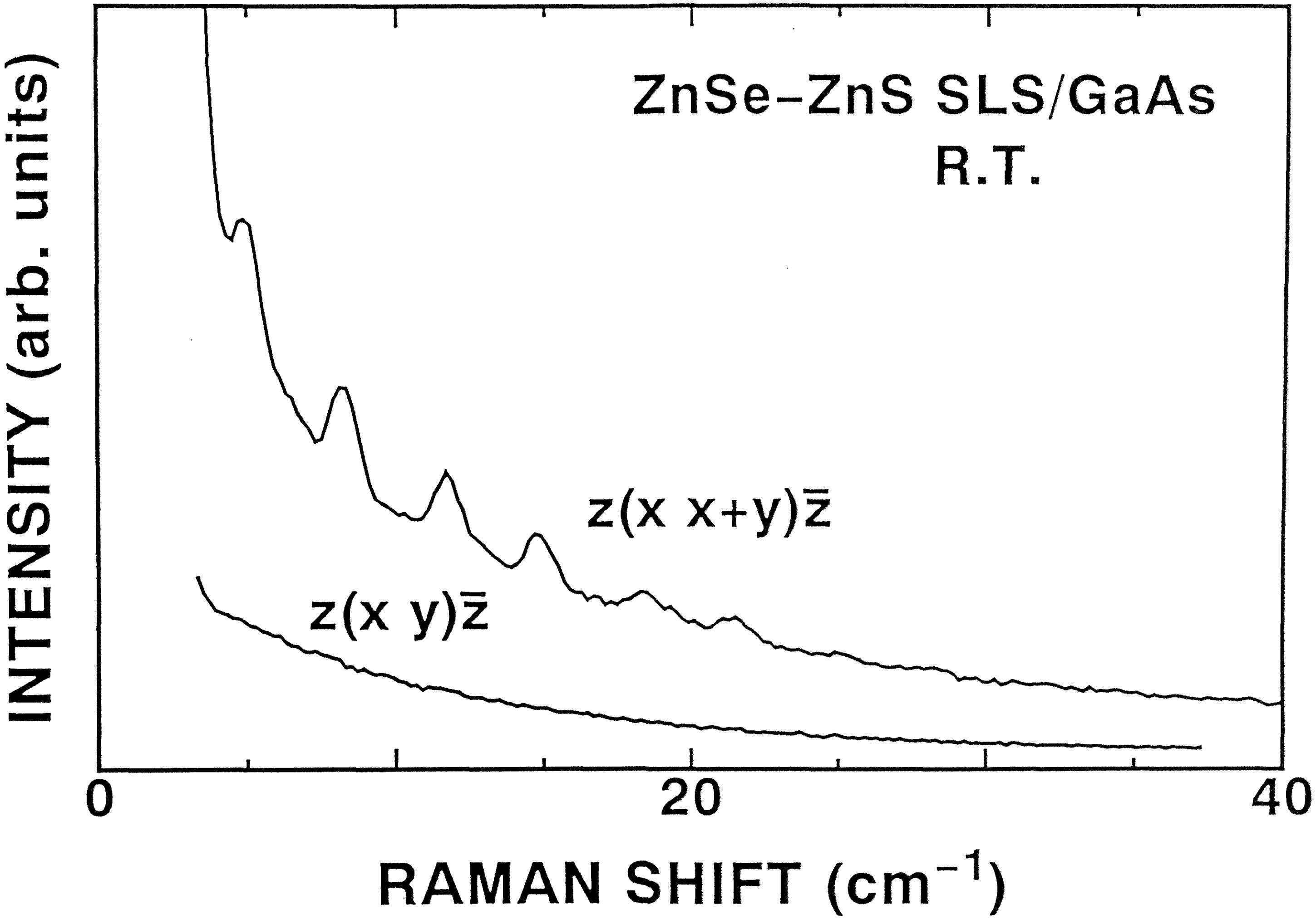

Fig. 4.1. Polarization dependence of Raman spectra of zone–folded modes. All the zone–folded modes are allowed only in $z(x,x)\bar{z}$ configuration, where x and y denote the polarization of the incident and scattered light (x//<100>, y//<010>).

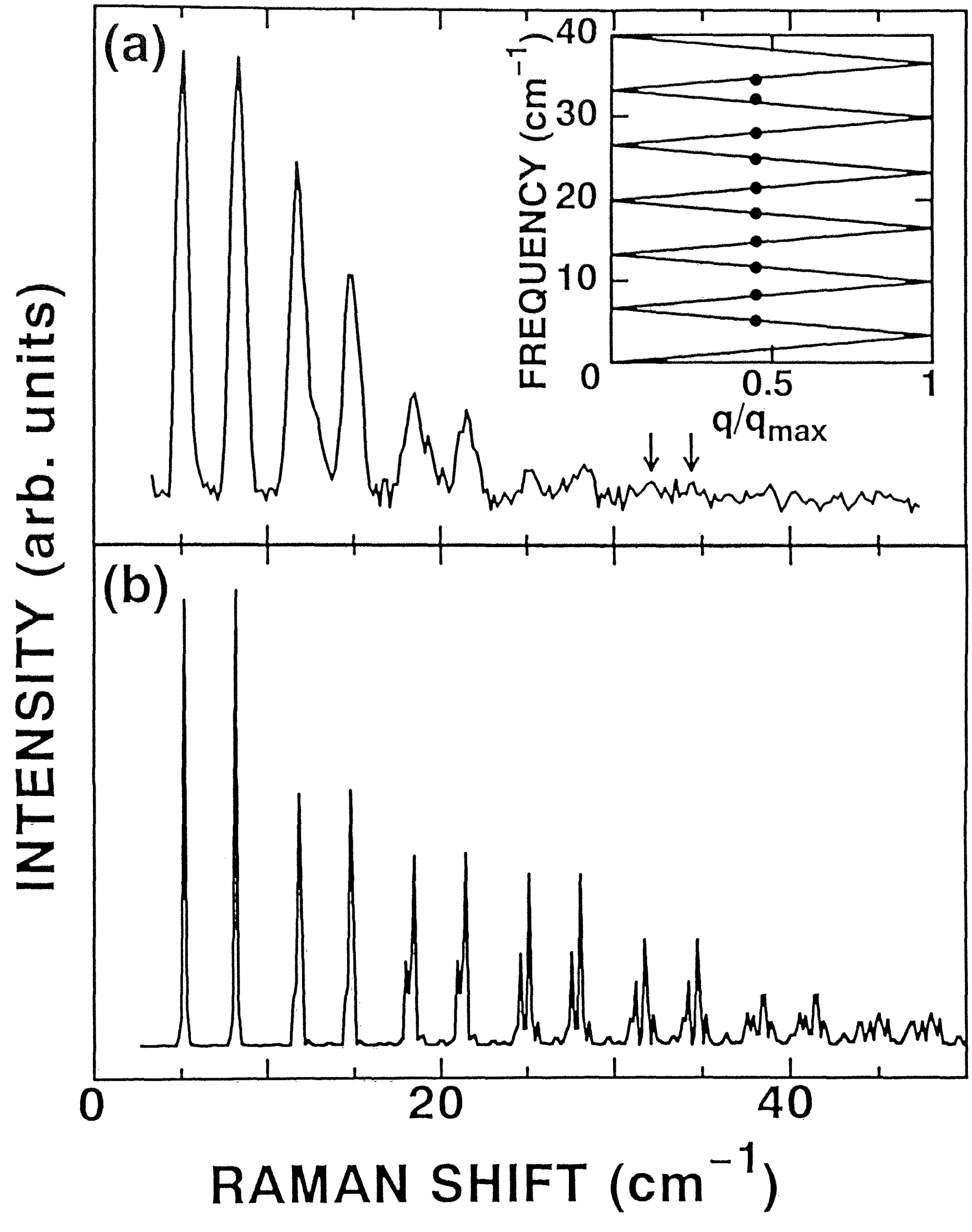

Fig. 4.2. Observed (a) and calculated (b) Raman spectra of zone-folded modes. The arrows show the peak positions of the fifth-order folded modes. Inset is phonon dispersion using conventional Rytov model, where q_{max} is the zone-edge wavevector π/d and d is the superlattice period.

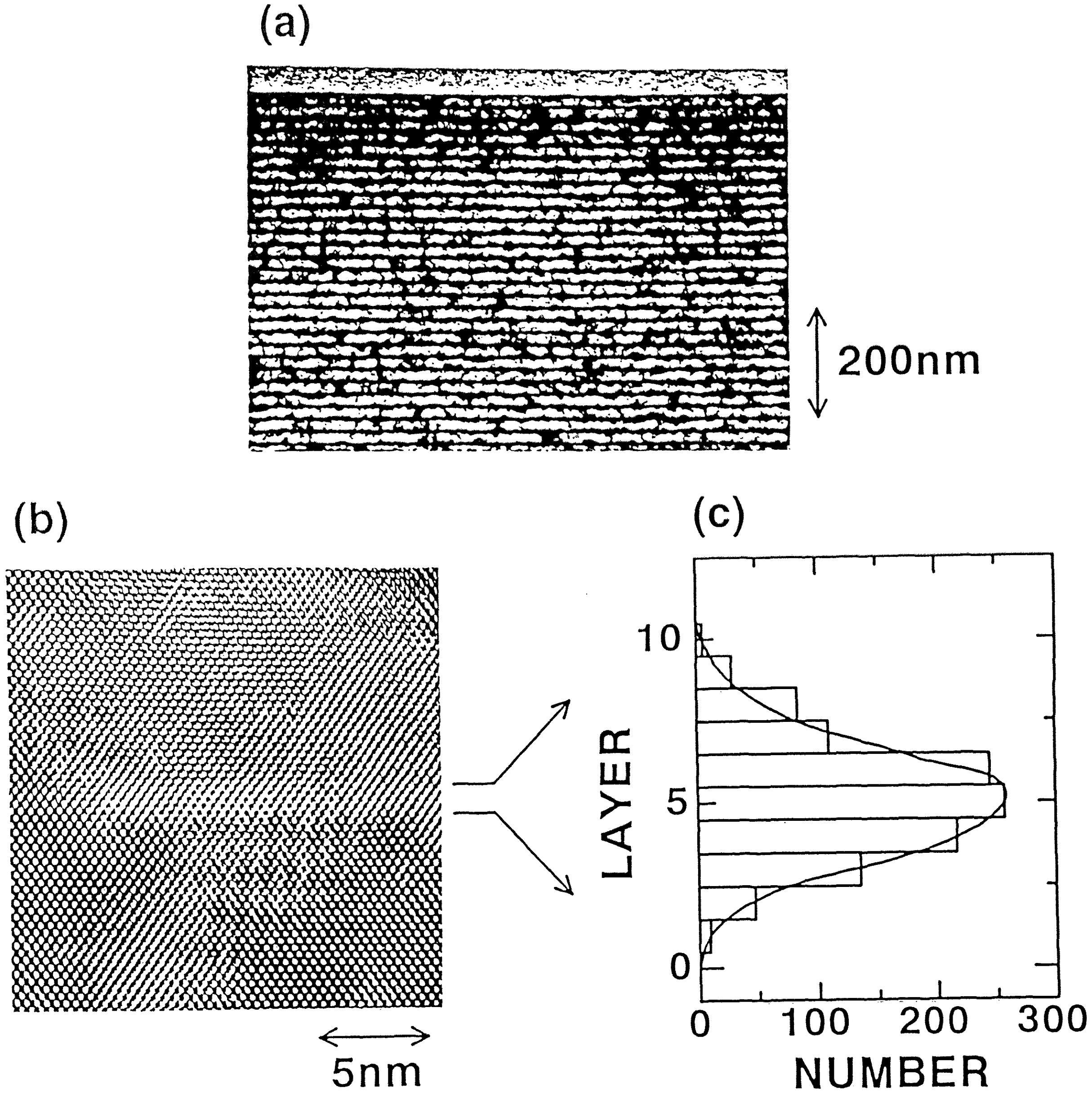

Fig. 4.3 Low- (a) and high- (b) resolution TEM images. (c) Histogram of the lattice points of ZnS. We obtained the each data in the histogram by counting the lattice points of ZnS along the straight arrays of lattice points parallel to the interface plane. The solid line is a guide to the eye.

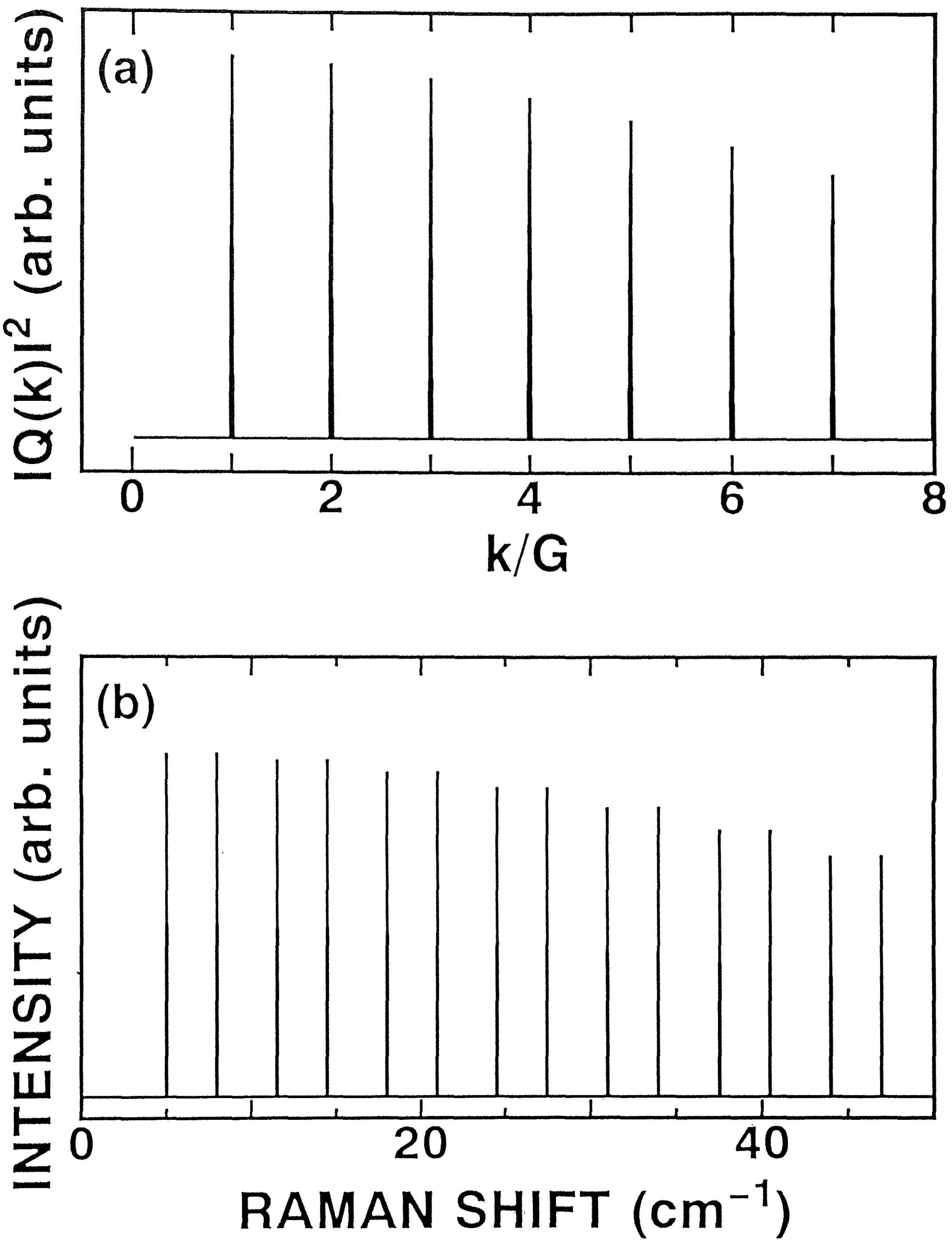

Fig. 4.4 (a) Fourier power spectrum of ideal sample structure (square-wave function). G is defined by $G = 2\pi/d$, where d is the superlattice period. (b) Calculated Raman spectra of zone-folded modes in an ideal sample structure.

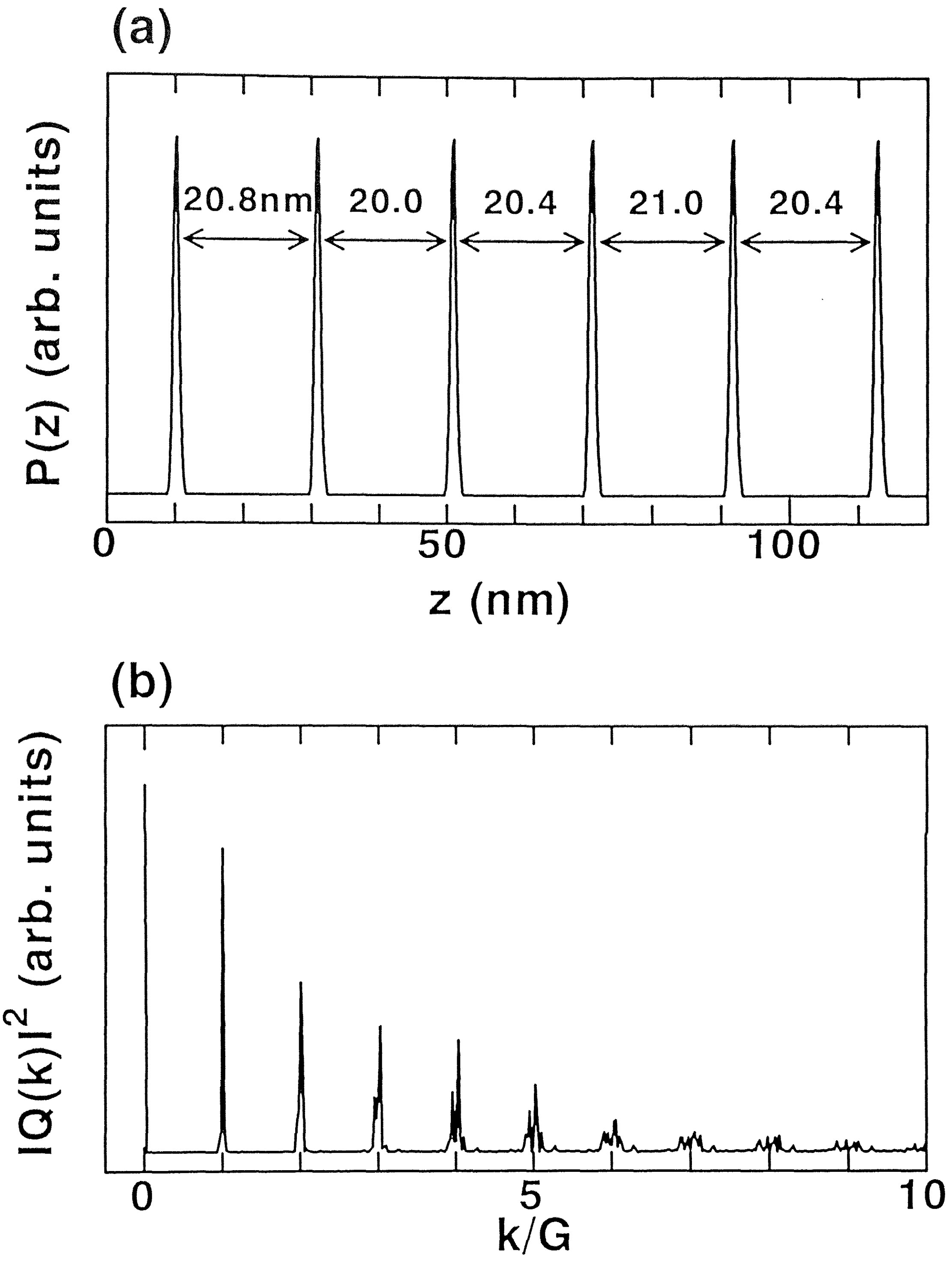

Fig. 4.5 (a) Photoelastic coefficient P(z) deduced from the TEM images. The intervals between the peak points are shown in the figure, showing the fluctuation of the periodicity. (b) Fourier power spectrum of P(z). G is defined by $G = 2\pi/d$, where d is the superlattice period.

CHAPTER V

BIAXIAL SPLITTING OF OPTICAL PHONON MODES

In Sect. 2.2.2 we have mentioned about the stress–induced peak shift of optical phonon in strained–layer superlattices. There exists a stress lying in the plane parallel to the interface. In this sense they have quasi–two–dimensional structures.

Many researchers have estimated the strains in the SLSs by means of Raman scattering.[1–6] All of the previous Raman studies of the strains measured the peak shifts of longitudinal optical (LO) phonons from bulk energies in a backscattering configuration with the incident light perpendicular to the interface plane. In this configuration, however, we cannot observe the directional stress directly. As mentioned in Sect. 2.2.2, the biaxial stress may induce the biaxial splitting of optical phonons. In order to find the biaxial splitting of the phonon modes, we newly measured Raman scattering with the incident light parallel as well as perpendicular to the interface plane. As a result, we were able to observe two types of phonon modes, that is a singlet and a doublet, for the first time.

5.1 Theoretical Prediction

In Sect. 2.2.2 we have shown that the splitting of optical phonon modes occurs because the biaxial stress makes the sample quasi–two–dimensional. In ZnSe–ZnS SLSs, Eq. (2.24) and parameters listed in Table 5.1 lead the relation $|\Delta\Omega_s| > |\Delta\Omega_d|$, for both the modes of ZnSe and ZnS.

When the incident and backscattered light are perpendicular to the interface plane (perpendicular configuration), the LO mode corresponds to the displacement of the atoms along the <001> direction [Fig. 5.1(b)]. Therefore, it will shift as the singlet type. On the other hand, the TO modes correspond to the displacement in the plane parallel to the interface. Therefore, it will shift as the doublet type. Thus in this experimental configuration, Eq. (2.24) indicates the energy deviations of the LO and TO modes as,

$$\begin{aligned}\Delta\Omega_s^{LO}&=[pS_{12}+q(S_{11}+S_{12})]X/\omega_0^{LO},\\ \Delta\Omega_d^{TO}&=[p(S_{11}+S_{12})+q(S_{11}+3S_{12})]X/2\omega_0^{TO}.\end{aligned} \tag{5.1}$$

We consider, next, the case where the incident and backscattered light are parallel to the <110> axis (parallel configuration). In this configuration, we can expect the LO mode will shift as the doublet type and the TO modes will split into the singlet and doublet types [Fig. 5.1(c)]. From Eq. (2.24) we can obtain,

$$\begin{aligned}\Delta\Omega_d^{LO}&=[p(S_{11}+S_{12})+q(S_{11}+3S_{12})]X/2\omega_0^{LO},\\ \Delta\Omega_s^{TO}&=[pS_{12}+q(S_{11}+S_{12})]X/\omega_0^{TO},\\ \Delta\Omega_d^{TO}&=[p(S_{11}+S_{12})+q(S_{11}+3S_{12})]X/2\omega_0^{TO}.\end{aligned} \tag{5.2}$$

To summarize the above mentioned expectation,[7] a) we will observe two types of shifts, a singlet and a doublet, of each of the LO and TO modes, corresponding to the two cases of the scattering configuration, and b) we will observe the singlet–type mode shifts larger than the doublet–type mode.

5.2 Experimental Results

We used three samples grown by low–pressure metalorganic chemical vapor deposition (MOCVD)[8] on (001) GaAs substrates. All the samples have the same thickness of ZnS layers (40 Å) and consist of 150 periods of the superlattice, while the thickness of ZnSe layers are different [(a) 15 Å, (b) 20 Å, (c) 25 Å]. We used a (110) cleavage plane for the parallel configuration measurement [Fig. 5.1(c)].

For the perpendicular configuration, the experiments were performed at room temperature by using a macro–Raman measurement system with the 4880 Å line of an Ar ion laser. For the parallel configuration, micro–Raman measurement system was used to focus the laser beam to the potion of the superlattice of the cleavage plane. Measurements were done at room temperature with the 5145 Å line of an Ar ion laser.

Figure 5.2 shows Raman spectra of samples (a), (b), and (c) in the perpendicular configuration. In Fig. 5.2, strong peaks of TO and LO modes of a GaAs substrate are observed at about 268 and 291 cm^{-1}. The dashed lines indicate the positions of the unstrained bulk ZnSe and ZnS LO modes. Very weak ZnSe TO modes are observed at about 210 cm^{-1}, although they are forbidden in this experimental configuration. As seen in the figure, ZnSe LO modes shift toward the higher energies, while ZnS LO modes shift toward the lower energies. This is because the ZnSe layers are under compressive stress and the ZnS layers are under tensile stress. Although the shift of the ZnSe LO mode in three samples does not differ from each other, the shift of the ZnS LO mode decreases with increasing ZnSe thickness. These observations are consistent with the previous works.[1-6] As mentioned above, in the perpendicular configuration, we can regard the shift of LO modes as the singlet type and that of TO modes as the doublet type.

Raman spectra in the parallel configuration are shown in Figs. 5.3 and 5.4. The incident light was polarized perpendicular or parallel to the <001> axis. The doublet TO mode is allowed for both polarizations, while the singlet TO mode is allowed only for the perpendicular polarization. Taking into account this selection rule, we identified the peaks of 210 and 240 cm^{-1} as doublet TO (ZnSe) and singlet TO (ZnS), respectively. Very weak peaks of about 255 cm^{-1} are identified as the forbidden ZnSe LO (doublet) mode. We can see small peaks at about 220 cm^{-1} in Fig. 5.4. We identified them as the forbidden singlet TO (ZnSe) mode. It is allowed for the perpendicular polarization. However, it is not observed in Fig. 5.3. This is because the singlet TO (ZnSe) mode is superposed on the singlet TO (ZnS) mode. This identification is justified by the following reasons. First of all, the intensity of the 220 cm^{-1} mode increases with the increase in the thickness of the ZnSe layer. Thus the mode is of ZnSe. Second, because of the selection rule, the intensity of the mode is weaker than that of the doublet TO (ZnSe) mode.

5.3 Discussion

Based on the above mentioned identification, we can summarize the energy deviation of all the modes in Table 5.2. Table 5.2 shows the energy deviation from the energy of the bulk mode for the sample (c). As for ZnSe modes, we can observe the singlet–type and doublet–type shifts for both LO and TO modes induced by the biaxial stress. The singlet–type mode shifts larger than the doublet–type one as was expected. However, energy deviations are about 5 cm^{-1} lower than those calculated using Eqs. (5.1) and (5.2). It seems that the energy deviation of the compressive stressed layers tend to be lower than the calculated value. This tendency was also observed in other SLSs systems, although the reason has not been well explained.[5] The parameters p and q listed in Table 5.1 were estimated under the conditions of stress of the order of 10^9 dyn/cm^2. However, the stress of the samples used in this work is one order of magnitude larger. There may be some nonlinear terms in addition to the linear terms of p and q, which cannot be neglected in our highly stressed samples. This fact may be one of the reasons of the discrepancy between the experimental and the theoretical values of energy deviations.

On the other hand, for ZnS modes, we can also observe the singlet–type and doublet–

type LO modes. However, the shift of the singlet type is not larger than that of the doublet type. This strange behavior may be explained by the following dielectric continuum model. The dielectric continuum model[9] treats the superlattice as a layered dielectric continuum. This model shows that the optical phonon mode which propagates in the layer plane can appear at new energy level. The energy deviation varies with the change in the relative thickness of the two different dielectric layers. This effect enhances the energy deviation of the doublet-type LO (ZnS) mode. For this reason, the doublet-type LO (ZnS) mode can shifts larger than the singlet-type one.

5.4 Summary

Raman scattering of ZnSe-ZnS strained-layer superlattices with the incident light perpendicular and parallel to the interface plane. We observed for the first time two types of the optical phonon shift, a singlet and a doublet, induced by the biaxial stress. We obtained reasonable relations between the stress and the direction of the shift and between the layer thickness and the shift. The singlet-type mode shifts larger than the doublet-type mode for the ZnSe optical phonon modes. Not only strained-layer superlattices, but there are many systems having directional stress in semiconductor devices. The method of this work will become a new characterization tool for measuring the directional stress in these systems.

References

[1] M. Nakayama, K. Kubota, H. Kato, and N. Sato, Solid State Commun. **51**, 343 (1984).

[2] F. Cerdeira, A. Pinczuk, J. C. Bean, B. Batlogg, and B. A. Wilson, Appl. Phys. Lett. **45**, 1138 (1984).

[3] B. Jusserand, P. Voisin, M. Voos, L. L. Chang, E. E. Mendez, and L. Esaki, Appl. Phys. Lett. **46**, 678 (1985).

[4] S. Nakashima, Y. Nakakura, H. Fujiyasu, and K. Mochizuki, Appl. Phys. Lett. **48**, 236 (1986).

[5] L. H. Shon, K. Inoue, K. Murase, H. Fujiyasu, and Y. Yamazaki, Solid State Commun. **62**, 621 (1987).

[6] L. H. Shon, K. Inoue, O. Matsuda, K. Murase, T. Yokogawa, and M. Ogura, Solid State Commun. **67**, 779 (1988).

[7] In Eqs. (5.1) and (5.2), ω_0 may be the bare optical phonon energy due to spring constants only. However, in Refs.1 and 3–5, ω_0 has been treated conventionally as ω_{LO} or ω_{TO} in the calculation of the each energy shift. We followed the conventional treatment in Eqs. (5.1) and (5.2). Anyhow, our conclusion is not influenced at all, whichever values are used.

[8] Y. Yamada, T. Taguchi, and A. Hiraki, Tech. Rep. Osaka Univ. **39**, 211 (1989).

[9] C. Colvard, T. A. Gant, M. V. Klein, R. Merlin, R. Fischer, H. Morkoç, and A. C. Gossard, Phys. Rev. B **31**, 2080 (1985).

Table 5.1. Parameters for ZnSe and ZnS used in the calculation of Ω_s and Ω_d.

	ZnSe	ZnS
a (Å)	5.6687	5.4093
LO mode (cm^{-1})	252[a]	349[a]
TO mode (cm^{-1})	205[a]	271[d]
S_{11} (10^{-12} $dyn^{-1}cm^2$)	2.11[b]	1.89[e]
S_{12} (10^{-12} $dyn^{-1}cm^2$)	-0.78[b]	-0.72[e]
p (10^{28} s^{-1})	-0.41[c]	-0.39[e]
q (10^{28} s^{-1})	-0.59[c]	-0.99[e]
G (10^{11} dyn·cm^{-1})	2.91[b]	3.54[e]

[a] Present work.

[b] Landolt–Börnstein, *Numerical Data and Functional Relationships in Science and Technology* (Semiconductors —— Physics of II–VI and I–VII Compounds, Semimagnetic Semiconductors), edited by O. Madelung, M. Schulz, and H. Weiss (Springer, Berlin, 1982), Vol. 17(b), p.145.

[c] F. Cerdeira, C. J. Buchenauer, F. H. Pollak, and M. Cardona, Phys. Rev. B **5**, 580 (1972).

[d] W. G. Nilsen, Phys. Rev. **182**, 838 (1969).

[e] Reference 5.

Table 5.2. Observed energy deviation of the LO and TO modes from the energy of the bulk mode for the sample (c).

		ZnSe (cm^{-1})	ZnS (cm^{-1})
LO	singlet	+7.5	−14.0
	doublet	+2.5	−21.4
TO	singlet	+14.5	−35.8
	doublet	+6.7	——

(a)

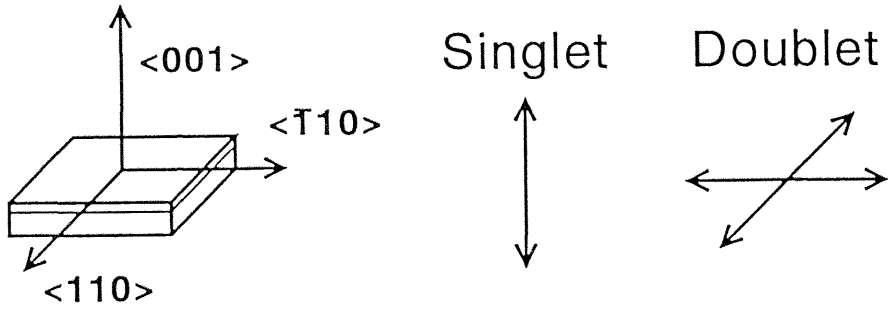

(b) Perpendicular Configuration

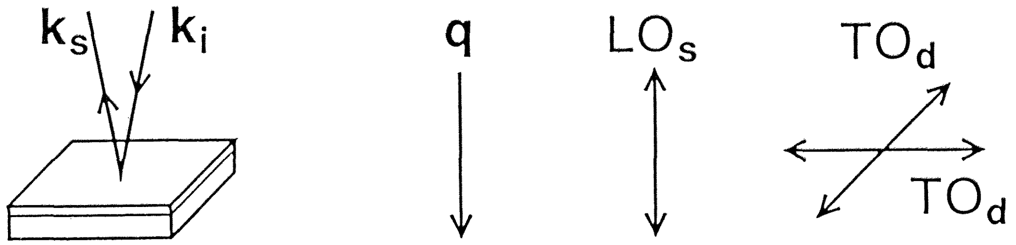

(c) Parallel Configuration

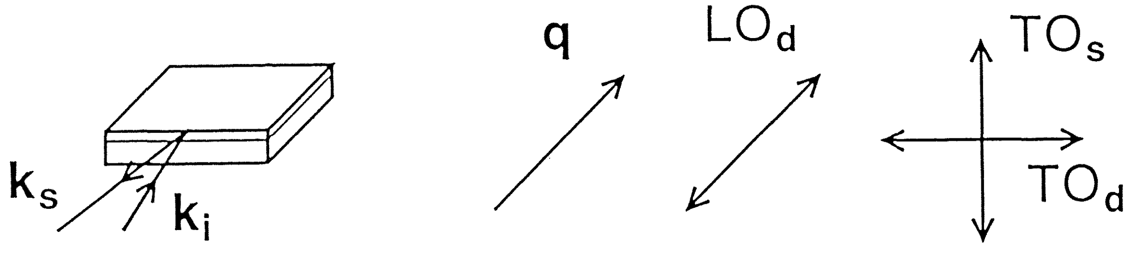

Fig. 5.1. (a) The relationship between the crystal axis and the vibrating direction of the singlet- and the doublet-type modes. Two types of measurement configurations were used: (b) perpendicular configuration and (c) parallel configuration. The subscripts of s and d denote a singlet and a doublet, respectively.

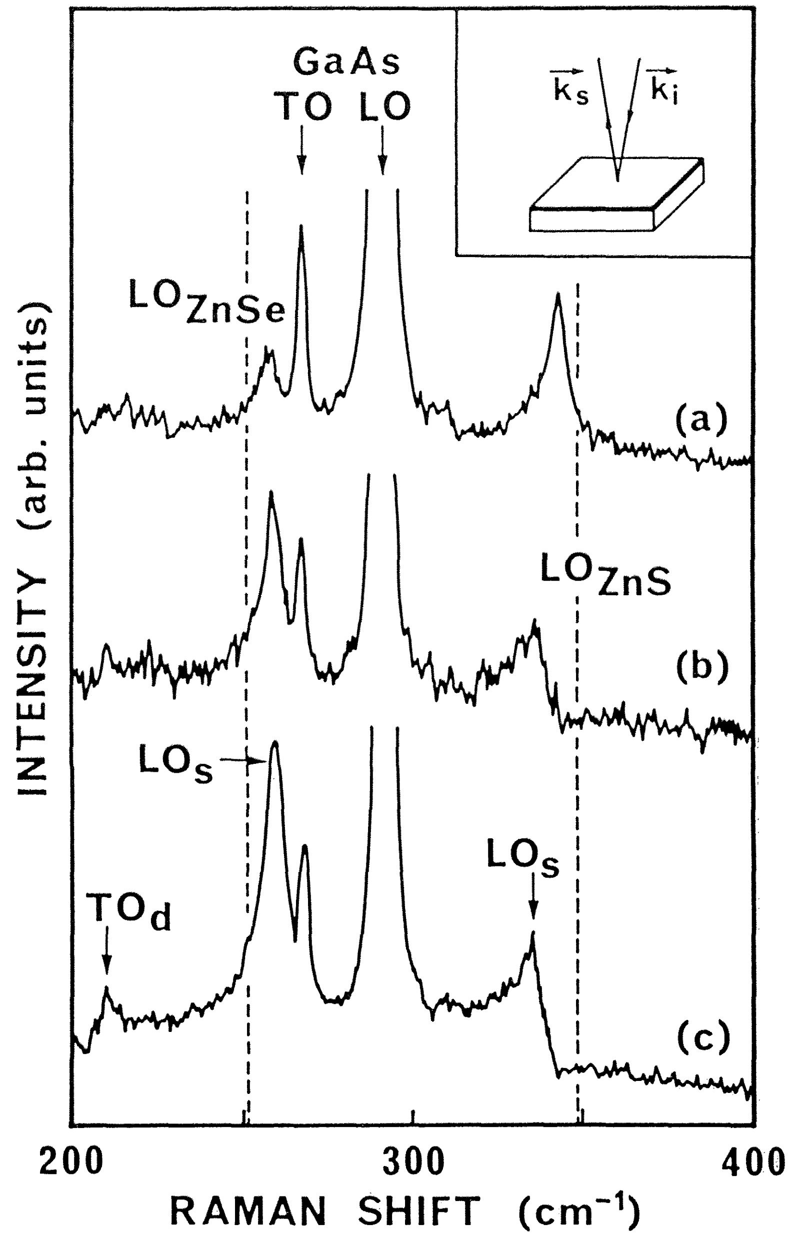

Fig. 5.2. Raman spectra of ZnSe–ZnS SLSs with a fixed ZnS layer thickness (40 Å) and various ZnSe ones [(a)15 Å, (b)20 Å, (c)25 Å]. The dashed lines show the unstrained bulk frequencies. The inset shows schematically the experimental configuration: the incident light is perpendicular to the (001) plane (perpendicular configuration). The subscripts of s and d denote a singlet and a doublet, respectively.

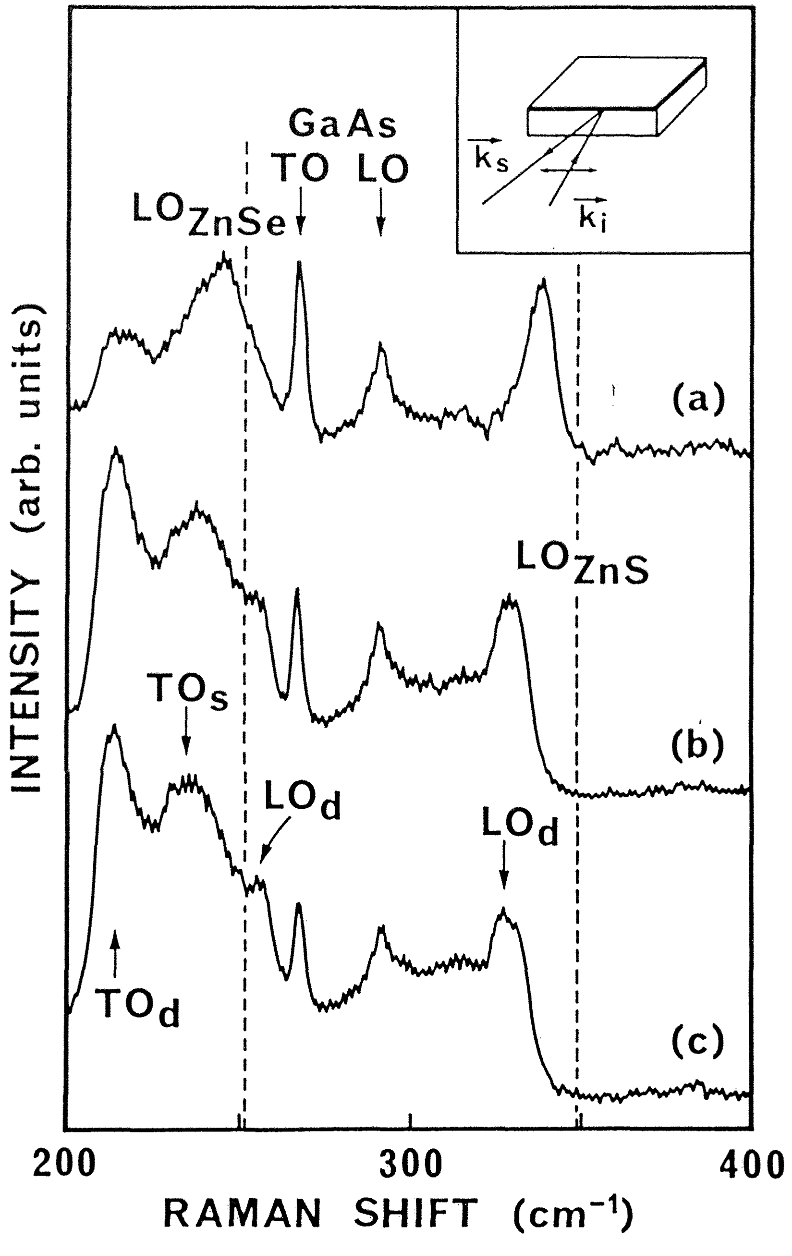

Fig. 5.3. Raman spectra of ZnSe–ZnS SLSs with a fixed ZnS layer thickness (40 Å) and various ZnSe ones [(a)15 Å, (b)20 Å, (c)25 Å]. The dashed lines show the unstrained bulk frequencies. The inset shows schematically the experimental configuration: the incident light is parallel to the <110> axis (parallel configuration) and is polarized perpendicular to the <001> axis. The subscripts of s and d denote a singlet and a doublet, respectively.

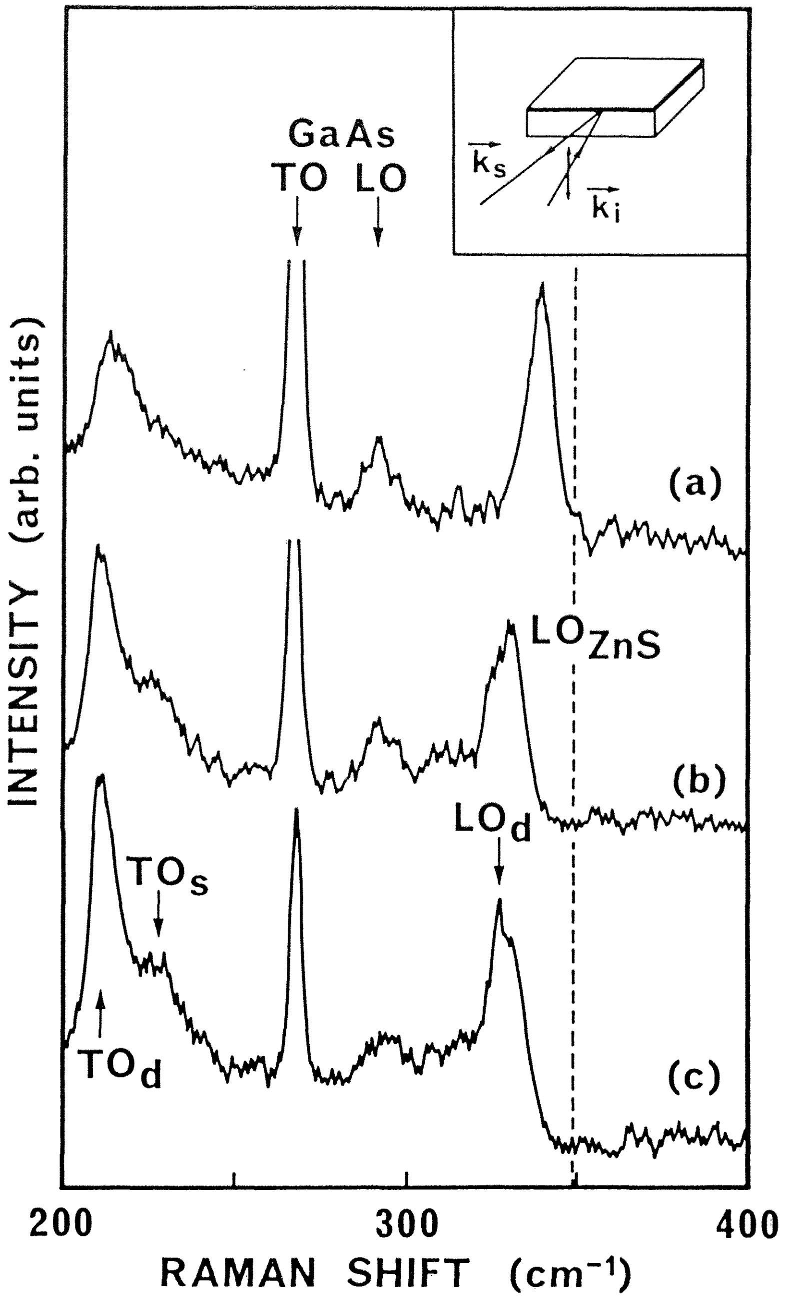

Fig. 5.4. Raman spectra of ZnSe–ZnS SLSs with a fixed ZnS layer thickness (40 Å) and various ZnSe ones [(a)15 Å, (b)20 Å, (c)25 Å]. The dashed line shows the unstrained ZnS energy. The inset shows schematically the experimental configuration: the incident light is parallel to the <110> axis (parallel configuration) and is polarized parallel to the <001> axis. The subscripts of s and d denote a singlet and a doublet, respectively.

CHAPTER VI

RAMAN PROFILE OF SUBMICRON-ORDER REGION

In Chap. V we studied the micro-Raman scattering from the sample with the spot size of ~1 μm in diameter. Generally, the spatial resolution is thought to be limited by the spot size of the laser beam at the sample surface.[1-3] As mentioned in Chap. III, the beam profile can be assumed to be a Gaussian shape and the spot size was estimated to be 1.3 μm in diameter. In this Chapter, we scan the position of the irradiated spot at intervals of ~0.1 μm and observed the submicron-order profile of Raman spectra in $Si_{0.5}Ge_{0.5}/Ge/Si_{1-x}Ge_x$ heterostructure. The results suggest that when we take account of the beam profile, we can observe the Raman signal from the submicron-order region of the sample.

6.1 Experimental Results

The samples used in this Chapter are $Si_{0.5}Ge_{0.5}/Ge/Si_{1-x}Ge_x$ heterostructures shown in Fig. 6.1. They were fabricated by molecular beam epitaxy (MBE) on (100) Ge substrates.[4] As the first growth step, a 500 nm thick buffer layer $Si_{1-x}Ge_x$ (x=0.68, 0.75, 0.80) was grown. The buffer layer is considered to be fully relaxed by leading misfit dislocations.[4] Next, a thin Ge channel (20 nm) and a thin $Si_{0.5}Ge_{0.5}$ cap (30 nm) layers were grown. The Ge channel layer is sandwiched by two SiGe alloy layers. Thus the Ge channel layer is under biaxial compressive stress due to the lattice mismatch.

Figure 6.2 shows the Raman spectra of three samples. These spectra were measured by using a macro-Raman measurement system with the 5145 Å line of an Ar ion laser at room temperature. One can notice four peaks. They are a Ge channel mode and three SiGe alloy modes, that is Ge–Ge (~300 cm^{-1}), Si–Ge (~400 cm^{-1}), and Si–Si (~470 cm^{-1}) bond vibration modes.[5,6] The peak positions of the Ge channel are 302, 305, and 306 cm^{-1} for the samples of x=0.80, 0.75, and 0.68, respectively. The phonon energies of the Ge channel are higher than the energy of triply–degenerated bulk Ge mode (301 cm^{-1}). With decreasing the composition x, the lattice mismatch between the buffer and Ge channel layers increases. Hence the compressive stress in the Ge channel increases and the stress–induced peak shift increases.

Next, we measured micro–Raman spectra of the cleavage surface of the sample x=0.68. We scanned the position of the irradiated spot from the surface side to the substrate side at scanning intervals of ~0.1 μm and obtained the Raman profile of the cross sectional structure of the sample. The typical results are shown in Fig. 6.3. As the value of "position" shown in Fig. 6.3 increases, the irradiated spot moves from the surface side to the substrate side. At the surface side, the Ge channel mode splits into singlet and doublet types (306, 303 cm^{-1}) induced by the biaxial stress. This fact is already discussed in Chap. V. As the irradiated spot moves to the Ge substrate side, the intensities of the Ge channel modes decrease and stress–free Ge substrate mode (301 cm^{-1}) becomes dominant.

6.2 Discussion

Figures 6.4 and 6.5 show the peak frequencies of each mode as a function of the position of the irradiated spot. The peak frequencies of two types of the Ge channel modes shift higher energy than that of the Ge substrate mode due to the biaxial stress. As the position of the irradiated spot moves to the Ge substrate side, the frequency of the Ge–Ge alloy mode increases while that of the Si–Si mode decreases. According to the experimental

Raman scattering results of SiGe alloy,[5,6] with increasing the composition of Ge, the frequency of the Ge–Ge mode increases while that of the Si–Si mode decreases. As for the Si–Ge mode, the frequency is at its maximum when the Ge concentration is about 50%. There are two alloy layers in our sample where the composition of Ge in the buffer layer is higher than in the cap layer. Hence as the irradiated spot moves to the substrate side, the signal from the buffer layer increases, the frequency of the Ge–Ge mode increases and those of the Si–Si and Si–Ge modes decrease. However, Fig. 6.4 shows that as the irradiated spot moves to the substrate side, Si–Ge mode shifts lower energy side and has its minimum at the "position" of 1 μm. The peak energy then increases slowly. The reason why the frequency of the Si–Ge mode does not decrease monotonously can be explained as follows. It is suggested that the segregation of Ge atoms occurs during the growth of the alloy layer.[7] Therefore, Ge composition becomes higher at the surface side in the buffer layer. Thus the frequency of the Si–Ge mode in the buffer layer is higher at the substrate side than at the surface side.

Figure 6.6 shows the peak intensity of each modes as a function of the position of the irradiated spot. Figure 6.7 shows the intensity ratios of Si–Si and Si–Ge modes to the Ge–Ge mode. Both of them decreases as the irradiated spot moves to the substrate side. The concentration of Ge in the buffer layer is larger than in the cap layer, consequently the density of Ge–Ge bond is larger. Then the intensity ratios of both the Si–Si and Si–Ge modes decrease.

The dependence of the intensity on the position of the irradiated spot is thought to be reflected both the structural profile of the sample and the laser beam profile. Let us define the function f(x), g(x), and I(x) as the profile of the sample structure, the profile of the laser beam, and the Raman intensity, respectively. Here x denotes the position. The detailed profile of f(x) will be described later. The Raman intensity I(x) can be expressed as the convolution of f(x) and g(x):

$$I(x) = \int_{-\infty}^{+\infty} f(x')g(x'-x)dx'. \tag{6.1}$$

Figure 6.8 shows the case for the calculation of the intensity of Ge substrate. The structural function of the Ge substrate can be expressed as a step function. As discussed in Chap. III, the laser beam profile can be assumed to be a Gaussian shape with the full width at half maximum (FWHM) 1.3 μm. In this case the Raman intensity I(x) shows an error function.

As for the calculation of the alloy mode, we considered the difference of the compositions of Si and/or Ge of the two alloy layers. For example, let us consider the profile f(x) of the Ge–Ge mode. Since the Ge–Ge mode corresponds to the vibration of the Ge–Ge bond, the Raman intensity of this mode is thought to be proportional to the density of Ge–Ge bond in the alloy layers. Hence f(x) can be given by

$$f(x) = \begin{cases} 0.5\times 0.5 = 0.25 & (-0.30 \le x \le -0.27 \text{ :cap layer}) \\ 0 & (-0.27 < x < -0.25) \\ 0.68\times 0.68 = 0.4624 & (-0.25 \le x \le 0.25 \text{ :buffer layer}) \\ 0 & (x < -0.30, x > 0.25). \end{cases} \tag{6.2}$$

Here we define the center of the $Si_{0.32}Ge_{0.68}$ buffer layer as the origin of position x. We calculate the intensities of each mode in this way. The results of the calculation are shown in Fig. 6.9. All the calculated intensity profiles reproduce the experimental results (Fig. 6.6) very well. The penetration depth of the sample is about 0.5 μm at the wavelength region of 5000 Å. Therefore we do not consider the dependence of the spot size on the depth.

6.3 Summary

We observed submicron-order profile of the Raman spectra by scanning the irradiated spot at intervals of ~0.1 μm. The Ge channel mode splits into singlet and doublet types induced by the biaxial stress. The dependence of Raman intensity and peak energy of alloy modes on the position of the irradiated spot is well understood by considering the difference of the composition of Ge in the two alloy layers. The calculations which consider the beam profile and the structural profile fully reproduced the dependence of the Raman intensity on the position of the irradiated spot. These results suggest that when we take account of the beam profile, we can observe the Raman signal from the submicron-order region of the opaque sample.

References

[1] J. B. Hopkins, L. A. Farrow, and G. J. Fisanick, Appl. Phys. Lett. **44**, 535 (1984).

[2] J. B. Hopkins and L. A. Farrow, J. Appl. Phys. **59**, 1103 (1986).

[3] S. Nakashima, K. Mizoguchi, Y. Inoue, M. Miyauchi, A. Mitsuishi, T. Nishimura, and Y. Akasaka, Jpn. J. Appl. Phys. **25**, L222 (1986).

[4] H. Etoh, E. Murakami, A. Nishida, K. Nakagawa, and M. Miyao, Jpn. J. Appl. Phys. **30**, L163 (1991).

[5] W. J. Brya, Solid State Commun. **12**, 253 (1973).

[6] G. M. Zinger, I. P. Ipatova, and A. V. Subashiev, Fiz. Tekh. Poluprovodn. **11**, 656 (1977) [Sov. Phys. Semicond. **11**, 383 (1977)].

[7] K. Nakagawa and M. Miyao, J. Appl. Phys. **69**, 3058 (1991).

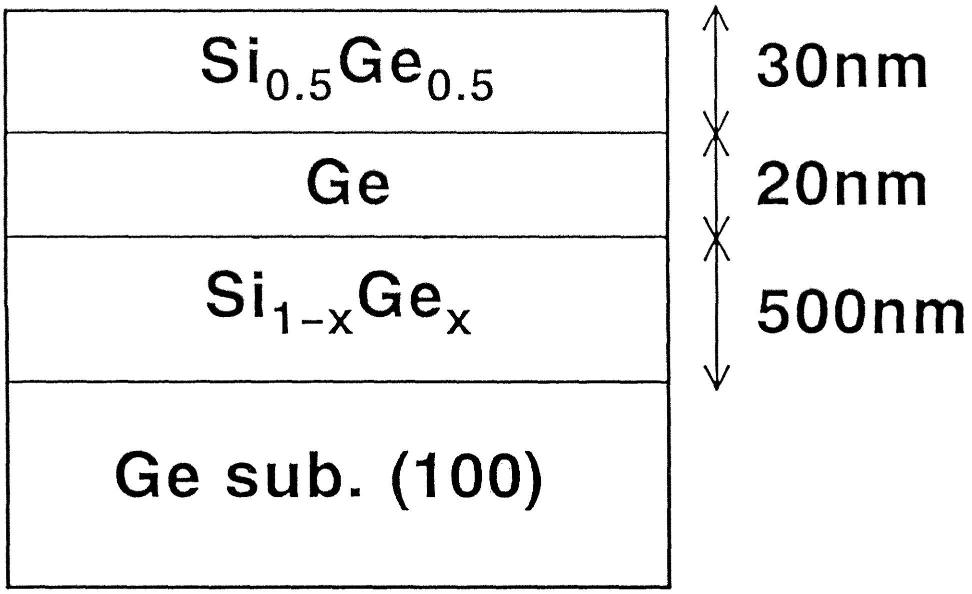

Fig. 6.1. Schematic cross section of the $Si_{0.5}Ge_{0.5}/Ge/Si_{1-x}Ge_x$ heterostructure. Three samples of x=0.68, 0.75, and 0.80 were used. The Ge channel layer is sandwiched by SiGe alloy layers and is under biaxial compressive stress.

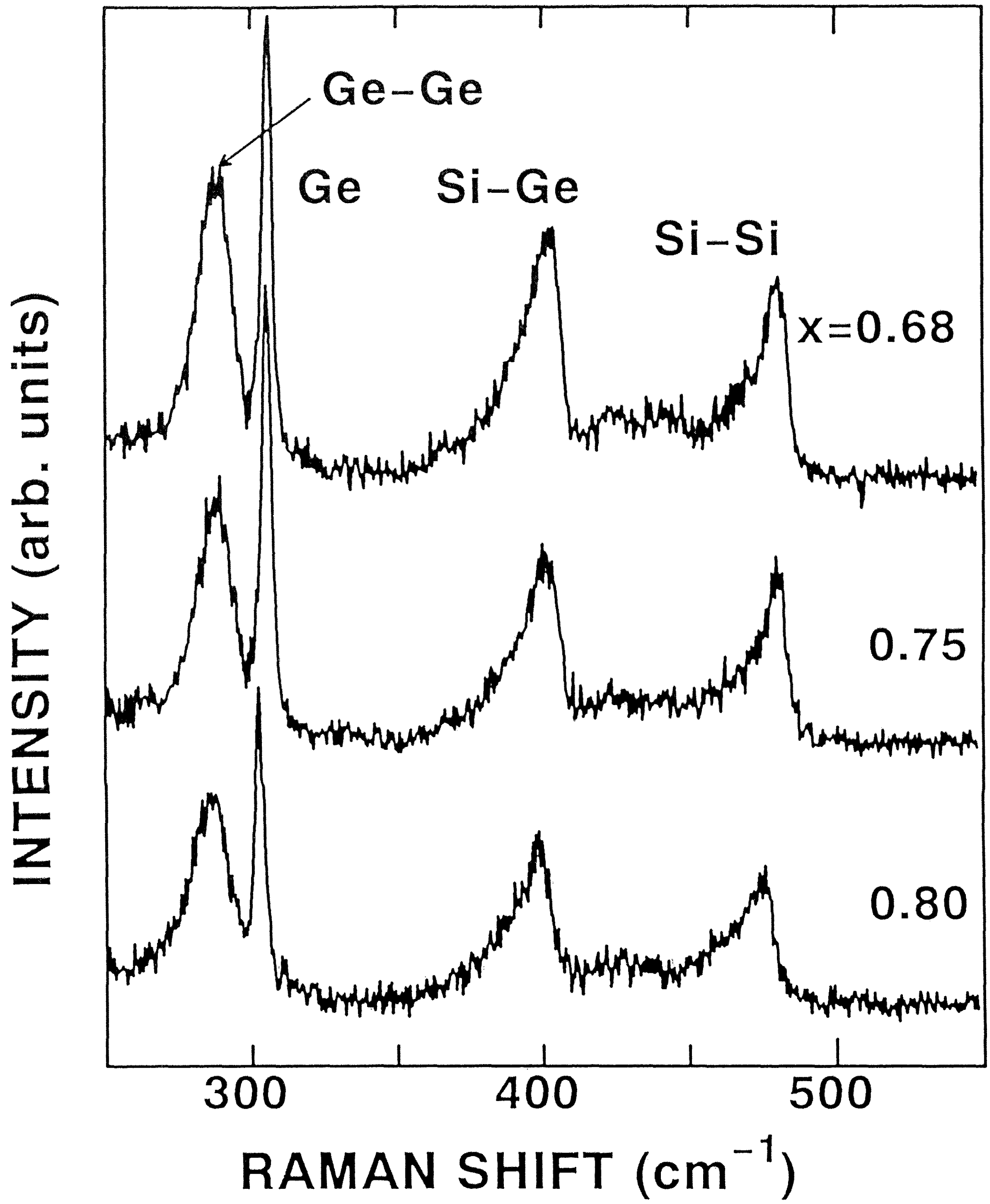

Fig. 6.2. Raman spectra of $Si_{0.5}Ge_{0.5}/Ge/Si_{1-x}Ge_x$ heterostructures varying the Ge composition (x=0.68, 0.75, 0.80). The Ge channel mode (~305 cm^{-1}) and three alloy modes (Ge–Ge, Si–Ge, Si–Si) were observed.

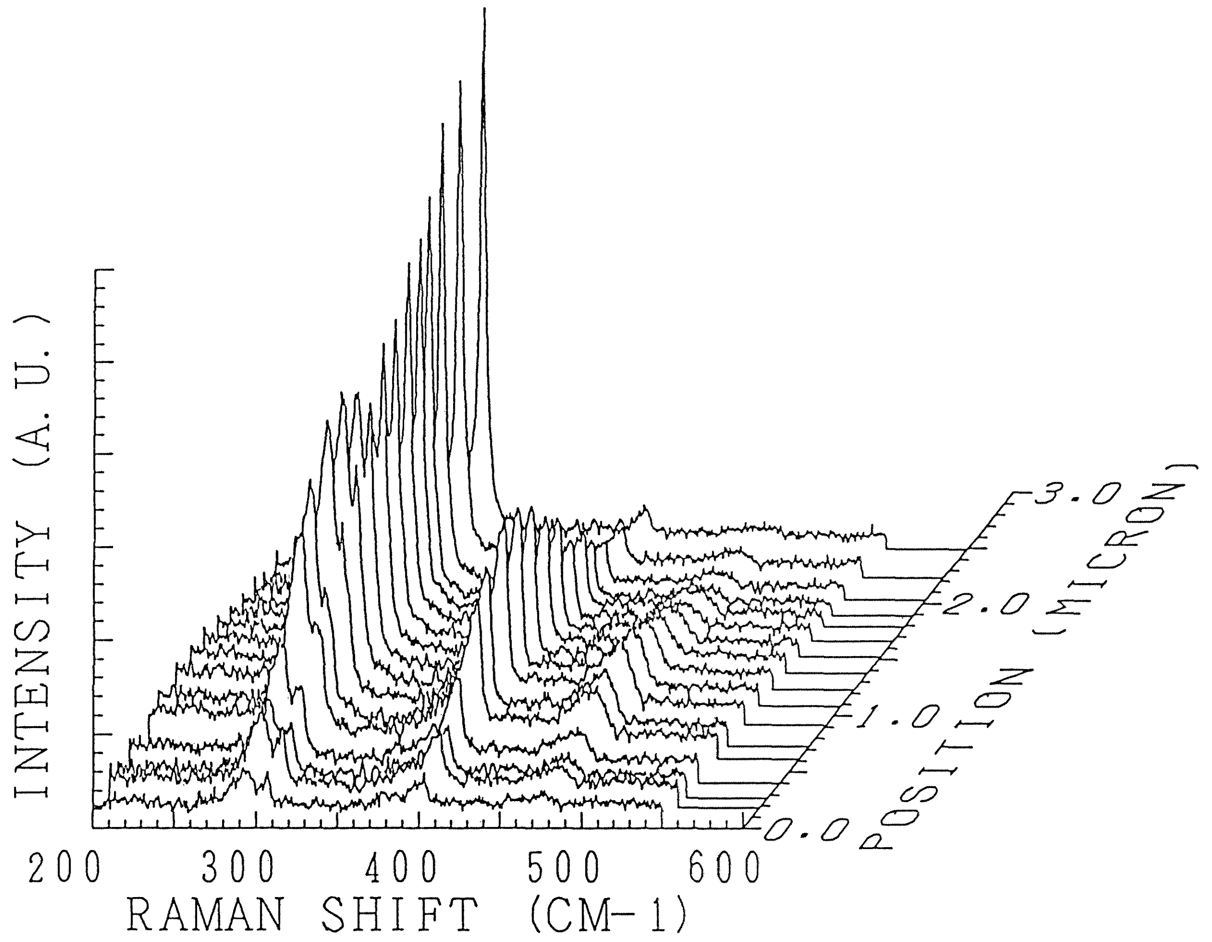

Fig. 6.3. Cross-sectional micro-Raman profile of $Si_{0.5}Ge_{0.5}/Ge/Si_{0.32}Ge_{0.68}$ heterostructure. As the value of "position" in the figure increases the irradiated spot moves from the surface side to the substrate side.

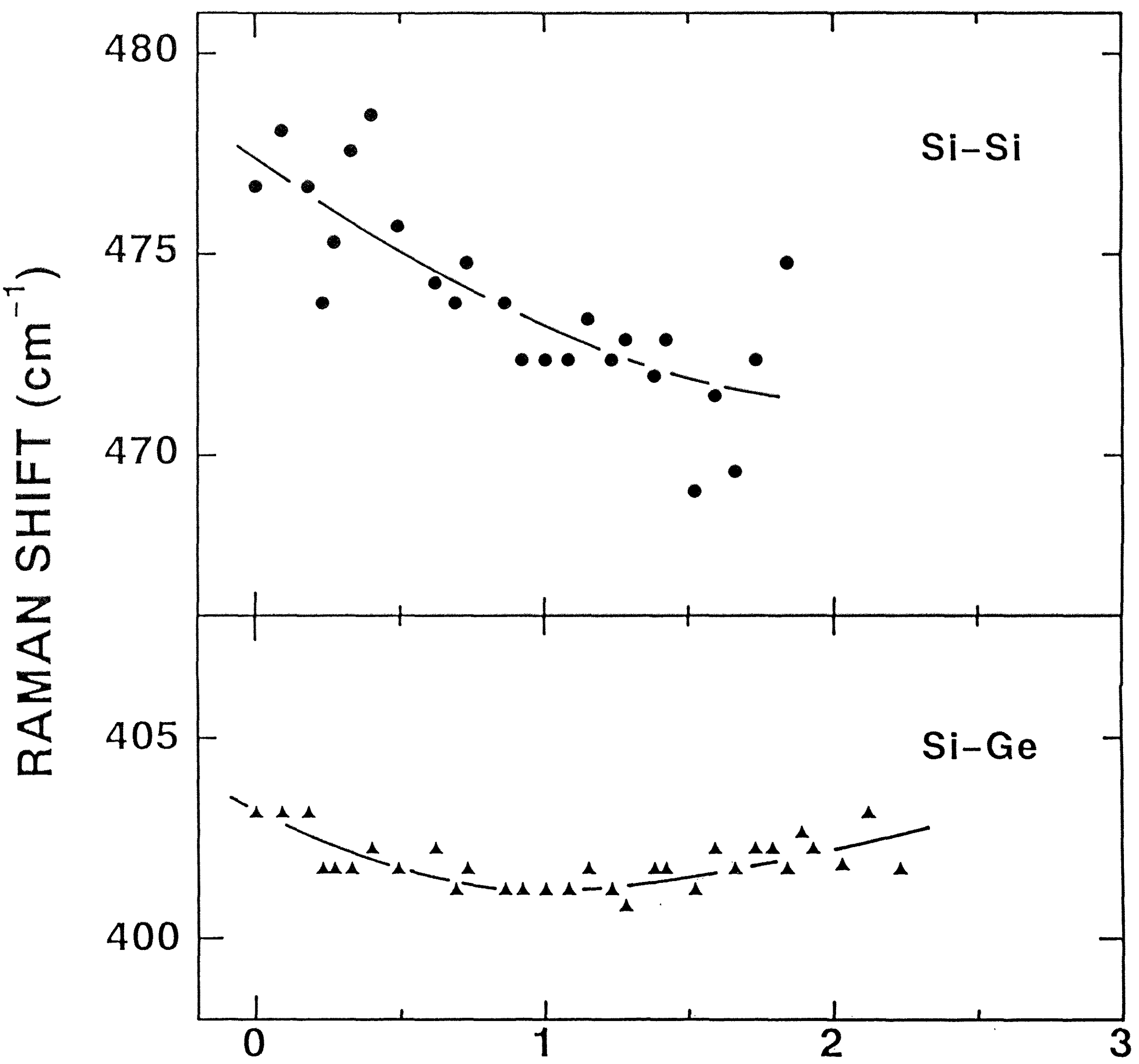

Fig. 6.4. The peak frequencies of Si–Si and Si–Ge modes as a function of the position of the irradiated spot. The solid lines are the guide to the eye.

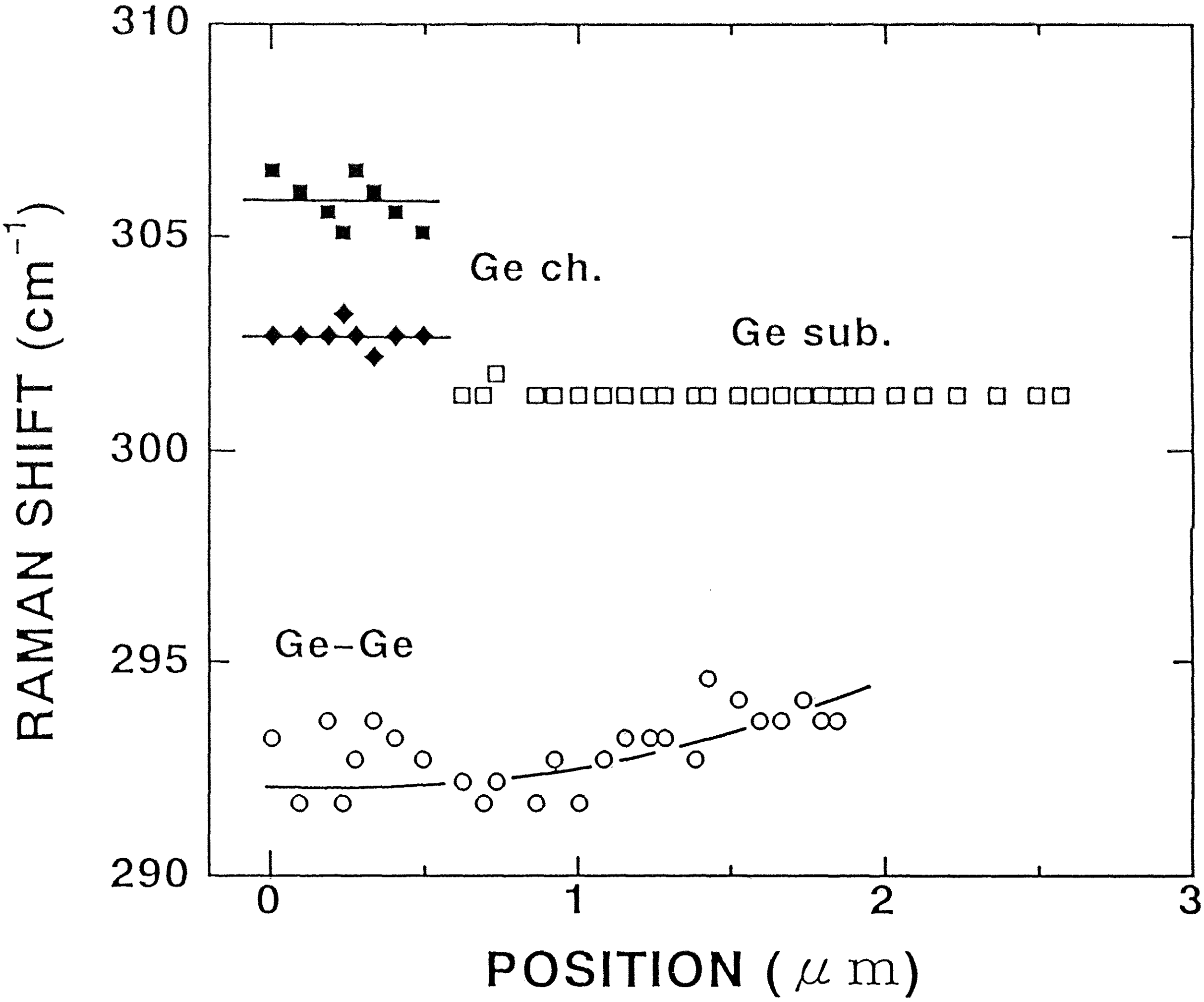

Fig. 6.5. The peak frequencies of Ge channel, Ge substrate, and Ge-Ge modes as a function of the position of the irradiated spot. The solid lines are the guide to the eye.

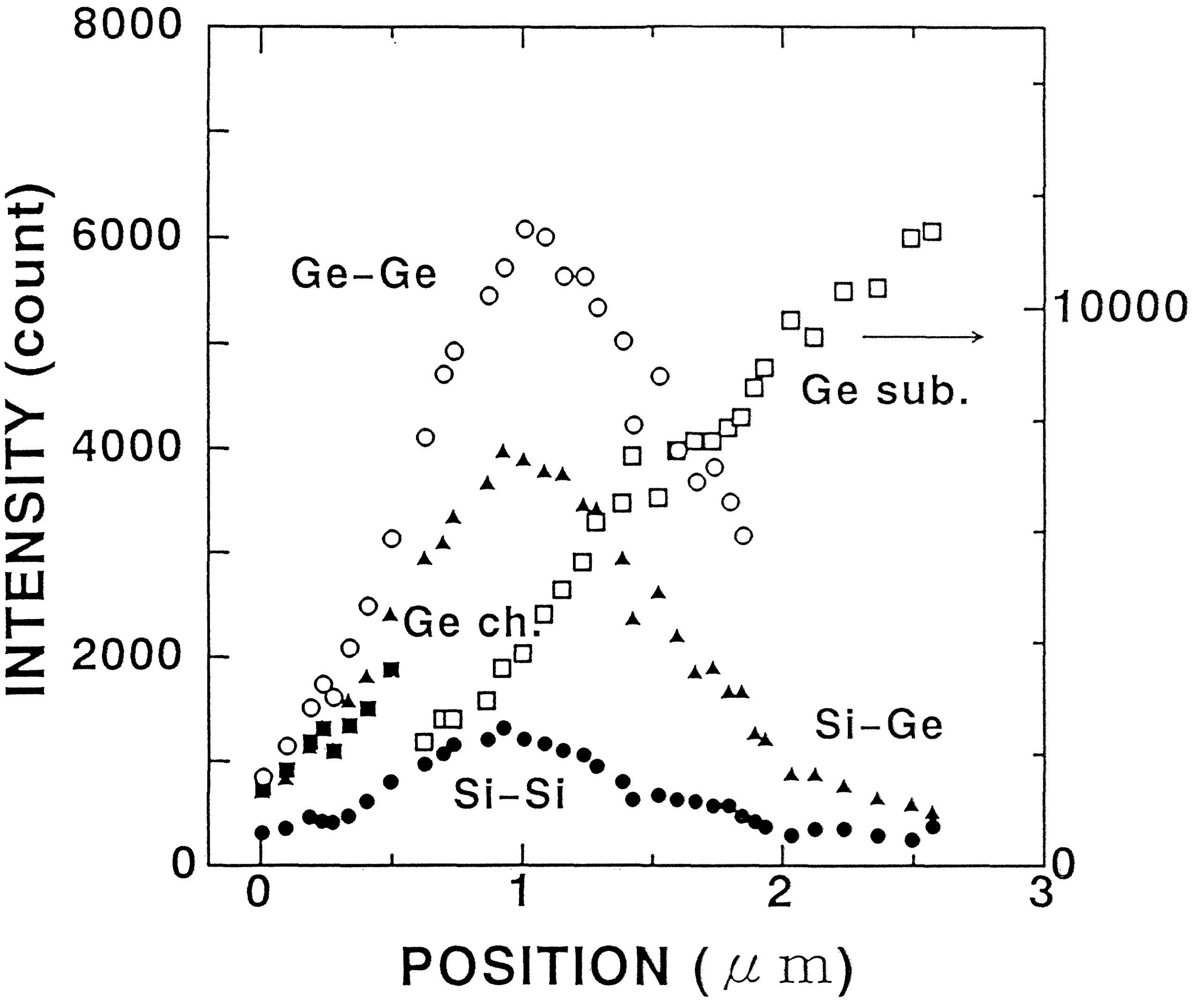

Fig. 6.6. The intensities of each modes as a function of the position of the irradiated spot.

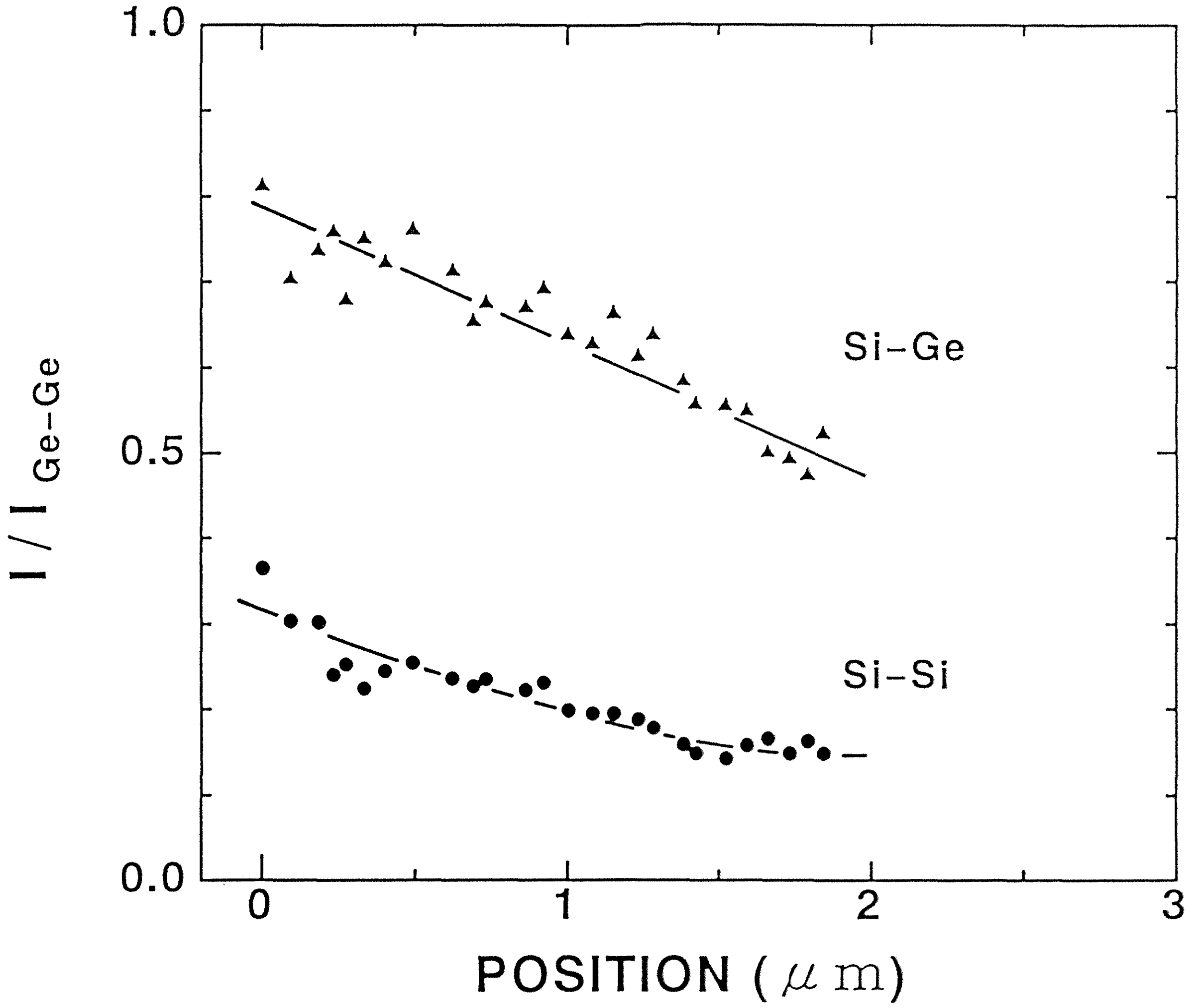

Fig. 6.7. The intensity ratios of the Si–Ge and Si–Si modes to the Ge–Ge mode as a function of the position of the irradiated spot. The solid lines are the guide to the eye.

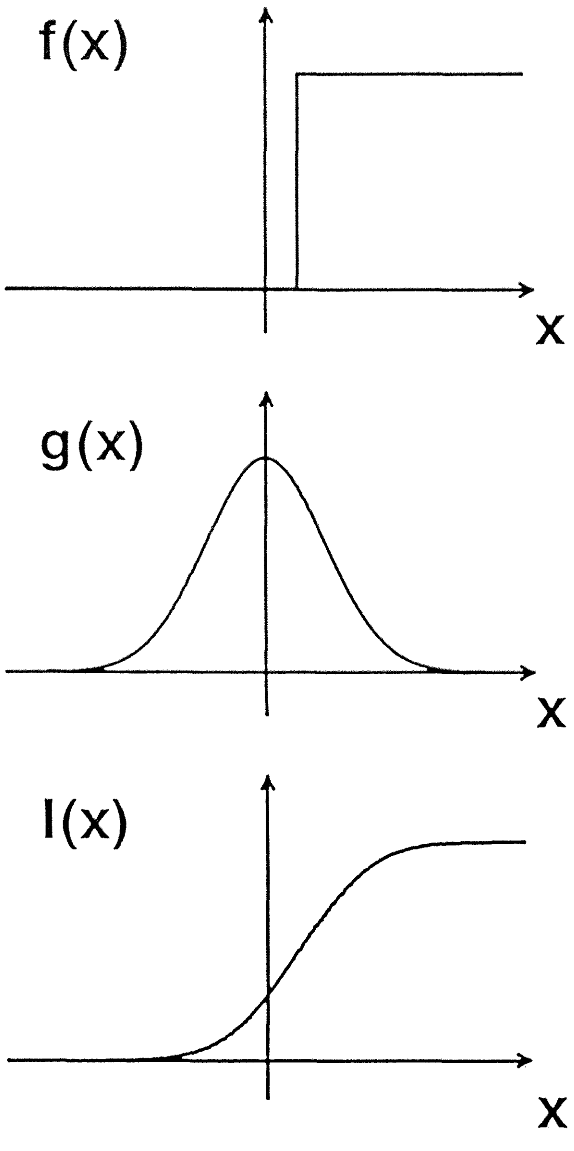

Fig. 6.8. The profiles of the functions f(x), g(x), and I(x) for the calculation of the intensity of Ge substrate. The functions f(x), g(x), and I(x) are the sample structure, laser beam profile, and Raman intensity, respectively (see text).

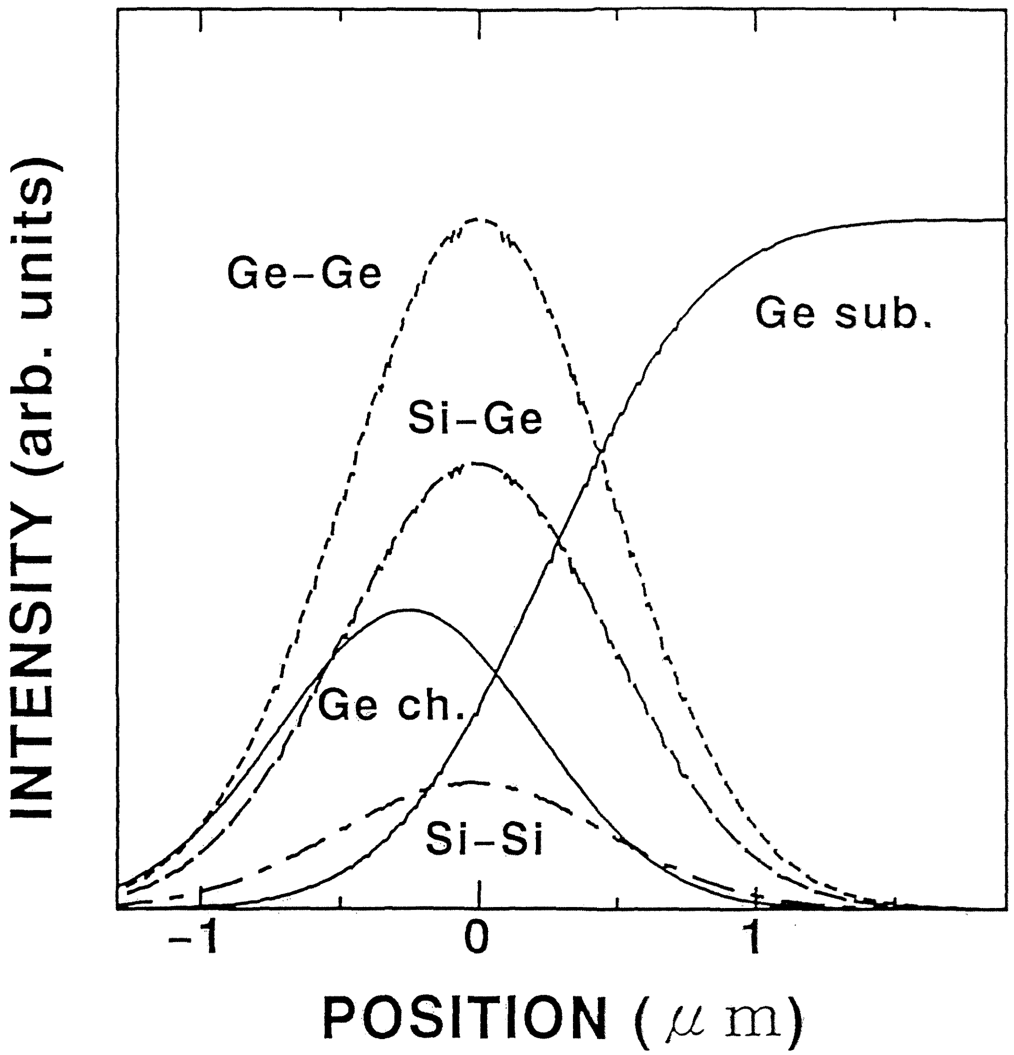

Fig. 6.9. Calculated intensities of each mode as a function of the position of the irradiated spot.

CHAPTER VII

PHONON CONFINEMENT IN SILICON NANOCRYSTALS

So far, we have discussed the Raman scattering from two–dimensional structures. In ZnSe–ZnS SLSs and SiGe heterostructures, the strain effect is dominant and phonon confinement effect was not clearly observed. This is because the lattice vibrations are confined only in one–dimension and the confinement effect is small. On the contrary, in nanocrystals, though it is not easy to control the nanocrystal size and crystallinity, three–dimensional confinement is realized and it is easier to study the confinement effect.

In this chapter, the effect of optical–phonon confinement is studied by means of Raman scattering spectroscopy. Most of the nanocrystals studied in the previous works are embedded in glass matrices.[1-5] Therefore, extrinsic effects such as strain between nanocrystals and matrices can not be neglected. It is desirable to prepare nanocrystals free from the extrinsic effects. We prepared Si nanocrystals fabricated by a gas break–down method.[6] These samples are expected to be free from the extrinsic effects. Hayashi, *et al.*[7,8] also studied Si and Ge nanocrystals fabricated by the gas evaporation technique. However, they observed a large amorphous–like Raman modes in small–size nanocrystals and the confinement effect was not discussed qualitatively.

The Raman spectrum of bulk Si exhibits a single peak at 521 cm^{-1}, which corresponds to the triply degenerate optical phonons at the center of the Brillouin–zone. In Si nanocrystals, the $q=0$ selection rule is relaxed and we must consider phonons in the region of $q\neq0$. The LO and TO phonons are not degenerate at the region of $q\neq0$. Hence two dispersion curves should be considered, although this was not considered before.

Only the average size of nanocrystals has been previously taken into account to discuss the Raman spectra, however it is necessary to consider the size distribution as well as the average size for the precise understanding of the confinement effect. In this chapter we discussed the confinement effects of LO and TO phonon modes qualitatively considering the size distribution.

7.1 Experimental Results

The Si nanocrystals were fabricated on the glass substrate by using a gas–breakdown method with a Nd^{3+}:YAG pulse laser (1.064 μm, 10 ns, 200 mJ/pulse).[6] The particle size can be controlled by varying the pressure of the SiH_4 gas in the reactive chamber (#1: 10 Torr, #2: 15 Torr, #3: 20 Torr). Figure 7.1 shows the transmission electron microscopy (TEM) images of the Si nanocrystals and the nanocrystals show almost spherical. The size distributions of the Si nanocrystals are shown in Fig. 7.2. It is reported that the distribution of nanocrystals can be fitted by a log–normal function:[9,10]

$$f(L)dL=\frac{1}{L\sqrt{2\pi\sigma^2}}\exp\frac{-(\ln L-\mu)^2}{2\sigma^2}dL, \tag{7.1}$$

where L is a diameter of the nanocrystal and μ and σ are a scale and a shape parameters.[11] An average diameter d_{av} can be calculated by the following equation,

$$d_{av}=\int_{+0}^{\infty}Lf(L)dL=\exp(\mu+\sigma^2/2). \tag{7.2}$$

The solid curves in the Fig. 7.2 show the results of the fitting by the log–normal function. The size distributions are fitted very well and the average diameters of the samples #1, #2, and #3 are estimated to be 7.0, 10.0, and 13.3 nm, respectively. Figure 7.3 shows the high resolution TEM image of the sample #1. The lattice fringes can be clearly seen and the nanocrystals are covered by oxide layers.[6] The average thickness of the oxide layer is 1.6 nm. Thus the net sizes of the nanocrystals must be estimated by subtracting the oxide layer thickness and are 3.7 nm (#1), 6.7 nm (#2), and 10.0 nm (#3) for three samples. The stress between nanocrystals and their oxide layers are estimated to be 2×10^9 dyn/cm^2 from the data of a SiO_2 film on a Si substrate.[12] The optical phonon energy will shift approximately -1 cm^{-1} due to the stress. The typical energy shift due to the confinement effect is larger than 1 cm^{-1}. Hence we neglect the stress effect in the following discussion.

Raman studies were performed by means of a micro-Raman measurement system with the 5145 Å line of an Ar ion laser at room temperature. The Raman spectra of each sample were measured ten times and the positions of the irradiated spot were randomly selected. The averaged Raman scattering spectra of the Si nanocrystals are shown in Fig. 7.4. The samples show good crystallinity because no amorphous-like peak (~480 cm^{-1}) were observed. The peak energy of the optical phonon mode shifts lower than the bulk Si energy (521 cm^{-1}), and the spectral shape is asymmetric and broad. However, the spectrum of the smallest size sample (#1) does not shift larger than the sample #2 and the full width at half maximum (FWHM) is narrower. One can also notice the small shoulder at the lower energy side (510 cm^{-1}) of the sharp peak in the spectrum of the sample #1.

7.2 Discussion

So far, it has been believed that with decreasing the nanocrystal size, the peak position decreases and spectral shape becomes wider and asymmetric due to the phonon confinement effect. However the smallest-size sample #1 did not show such behaviors. Tsu *et al.*[13] studied Raman scattering in porous Si and observed two peaks at 510 and 518 cm^{-1}. They attributed the appearance of two peaks to a LO–TO splitting, however detailed discussion was not stated. The porous Si is thought to be a gathering of nanocrystals[14] and is similar to our sample. Following their attribution, we assign the sharp peak and the shoulder to LO and TO modes, respectively. We adopted a conventional model calculation of the phonon confinement to support the above assignment.

In Sect. 2.3 we discussed about a quantitative model calculation for nanocrystals by considering the phonon confinement effect which is expressed by Eq. (2.29). The spatial correlation (SC) model calculation shows the relationship between the correlation length, the peak shift, and the spectral shape. Previously, LO phonon dispersion curve of bulk Si alone has been used.[15] In order to explain the LO–TO splitting, we consider both the LO and TO dispersion curves and calculate the Raman spectra. The dispersion curves can be expressed as the from,

$$\omega(q)^2 = A + \sqrt{A^2 - B\{1 - \cos[(a/2)q]\}}, \tag{7.3}$$

which reproduces the dispersion curves of <111> direction.[16] The parameters A and B used here are A=1.36×10^5 (cm^{-2}) and B=7.96×10^9 (cm^{-4}) for LO mode and A=1.36×10^5 (cm^{-2}) and B=3.24×10^9 (cm^{-4}) for TO mode. The FWHM of the bulk phonon mode, Γ_0, used in the calculation was 3.6 cm^{-1} determined through our experiment. Figure 7.5 shows the calculated results of the energy shifts from the bulk energy as a function of the diameter of the nanocrystal. The solid and broken lines are the calculated energy deviations of LO and TO modes from the energy in bulk Si. With decreasing the nanocrystal size, the energy difference between LO and TO modes increases. Only one peak was observed in the samples #2 and #3. In our treatment, this result can be explained by considering that the energy difference between LO and TO modes is small and that LO and TO modes overlap to each other. When the particle size is small, the splitting value increases and two modes can be observed.

Next, we considered the size distribution in order to compare experimental data to the theoretical calculation. We calculated the LO phonon spectra by summing up the size-dependent spectrum weighted by the size distribution function (log-normal function):

$$I'(\omega)=\int I(\omega,L)f(L)dL, \tag{7.4}$$

where I'(ω) and I(ω,L) are the averaged spectrum and the spectrum of the size L, respectively. The function I(ω,L) is defined by Eq. (2.29). The broken lines in the Fig. 7.4 are the results of the above calculation. The calculated spectra of #2 and #3 agree very well to the experimental data. Whereas for the sample #1, the calculated spectrum does not reproduce the experimental data: Peak energy of the calculated spectrum is too low and spectral shape is too broad. As shown in Fig. 7.5, peak shift of the TO mode is smaller than that of LO mode. Therefore, if we consider both the LO and TO modes, the calculated spectrum will be improved.

However, when we used TO phonon dispersion curve and Eq. (2.29), the peak position is still lower and the FWHM is wider than the observed one. One reason of this discrepancy may be the confinement effect is smaller than that of LO phonon. We then fit the experimental spectrum by varying the confinement effect of TO mode. The weak tail of the lower energy side was fitted by superposing the LO phonon spectrum on the weakly-confined TO phonon spectrum. Figure 7.6 shows the result of the fitting. The dotted lines show LO and TO phonon spectra and the broken line shows the superposed spectrum. The TO phonon spectrum corresponds to the confined spectrum of the size of 75 nm. Although the fitted spectrum can not reproduce the shoulder, the broad weak tail of lower energy side is well reproduced.

Similar behavior was reported by Fujii *et al.*[3] in Ge nanocrystals. They reported that with decreasing the nanocrystal size, the peak energy shifts to lower energy side. However, when the size is less than 10 nm, the peak energy returns to the higher energy side. They discussed about this strange result and considered the stress effect, though clear answer was not obtained. They also observed a weak tail at the lower energy side of the main peak. From our treatment, the weak tail can be attributed to the LO mode and the main peak corresponds to the TO mode.

In the above discussion, the problem is why the TO mode becomes dominant as the size of nanocrystals decreases. The Raman spectrum of amorphous Si depends on the phonon density of states because of the complete relaxation of the q selection rule.[17] Hence the Raman spectrum of amorphous Si shows a rather broad TO mode with a weak shoulder of an LO mode at the lower energy side. In our Si nanocrystals the phonon confinement effects leads a relaxation of the q selection rule and the similar effect may be occur. Therefore, with decreasing the nanocrystal size, the spectral shape of the LO mode becomes broad and weak and the TO mode becomes dominant.

7.3 Summary

In this Chapter Raman scattering from Si nanocrystals were studied. The samples were fabricated by the gas break–down method and the nanocrystals were in almost stress–free condition. The Raman spectrum of the smallest nanocrystals showed the high energy peak shift and the narrowing of the spectral width. These anomalous behavior can be explained by the spatial correlation (SC) model which considers both the dispersion curves of LO and TO phonons. It is shown that as the size of nanocrystals decreases, the energy difference between LO and TO phonons increases, the LO phonon mode becomes broad and weak, and TO phonon mode becomes dominant. Our treatment of the phonon confinement effect can also reasonably explain the previous experimental results of the other authors.

References

[1] S. Vepřek, Z. Iqbal, H. R. Oswald, and A. P. Webb, J. Phys. C **14**, 295 (1981).

[2] Z. Iqbal and S. Vepřek, J. Phys. C **15**, 377 (1982).

[3] M. Fujii, S. Hayashi, and K. Yamamoto, Jpn. J. Appl. Phys. **30**, 687 (1991).

[4] A. Tanaka, S. Onari, and T. Arai, Phys. Rev. B **45**, 6587 (1992).

[5] G. Scamarcio, M. Lugará, and D. Manno, Phys. Rev. B **45**, 13792 (1992).

[6] T. Kawaguchi and S. Miyazima, Bull. Am. Phys. Soc. **37**, 719 (1992).

[7] S. Hayashi, M. Ito, and H. Kanamori, Solid State Commun. **44**, 75 (1982).

[8] S. Hayashi and H. Abe, Jpn. J. Appl. Phys. **23**, L824 (1984).

[9] C. G. Granqvist and R. A. Buhrman, Solid State Commun. **18**, 123 (1976).

[10] C. G. Granqvist and O. Hunderi, Phys. Rev. B **16**, 3513 (1977).

[11] A. M. Law and W. D. Kelton, *Simulation Modeling and Analysis*, (McGraw-Hill, New York, 1986), p.164.

[12] B. Leroy, Philos. Mag. B **55**, 159 (1987).

[13] R. Tsu, H. Shen, and M. Dutta, Appl. Phys. Lett. **60**, 112 (1992).

[14] M. W. Cole, J. F. Harvey, R. A. Lux, D. W. Eckart, and R. Tsu, Appl. Phys. Lett. **60**, 2800 (1992).

[15] I. H. Campbell and P. M. Fauchet, Solid State Commun. **58**, 739 (1986).

[16] R. Tubino, L. Piseri, and G. Zerbi, J. Chem. Phys. **56**, 1022 (1972).

[17] R. Alben, D. Weaire, J. E. Smith, and M. H. Brodsky, Phys. Rev. B **11**, 2271 (1975).

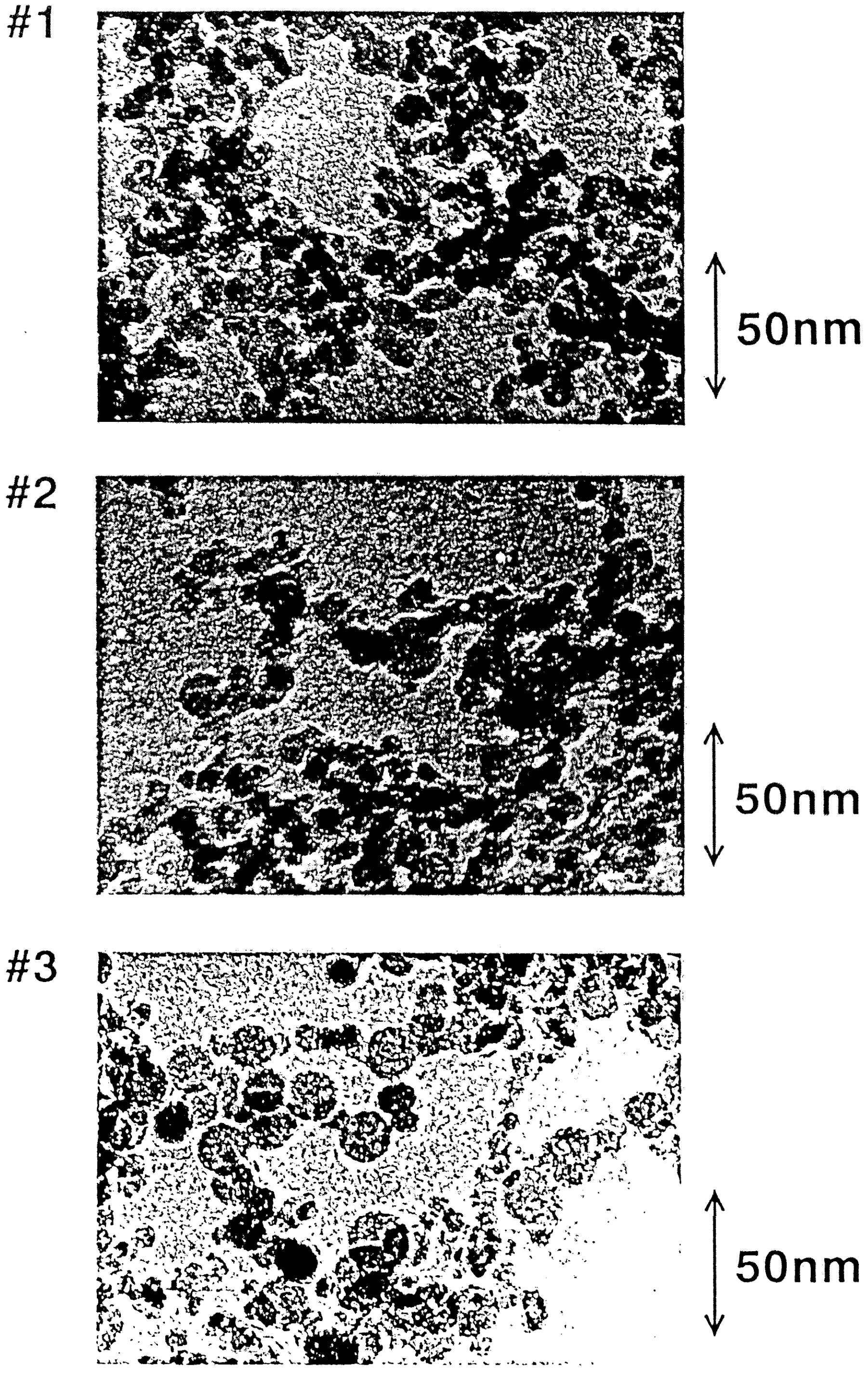

Fig. 7.1. TEM images of Si nanocrystals. The pressure of the SiH_4 gas was varied (#1: 10 Torr, #2: 15 Torr, #3: 20 Torr). The nanocrystals show almost spherical.

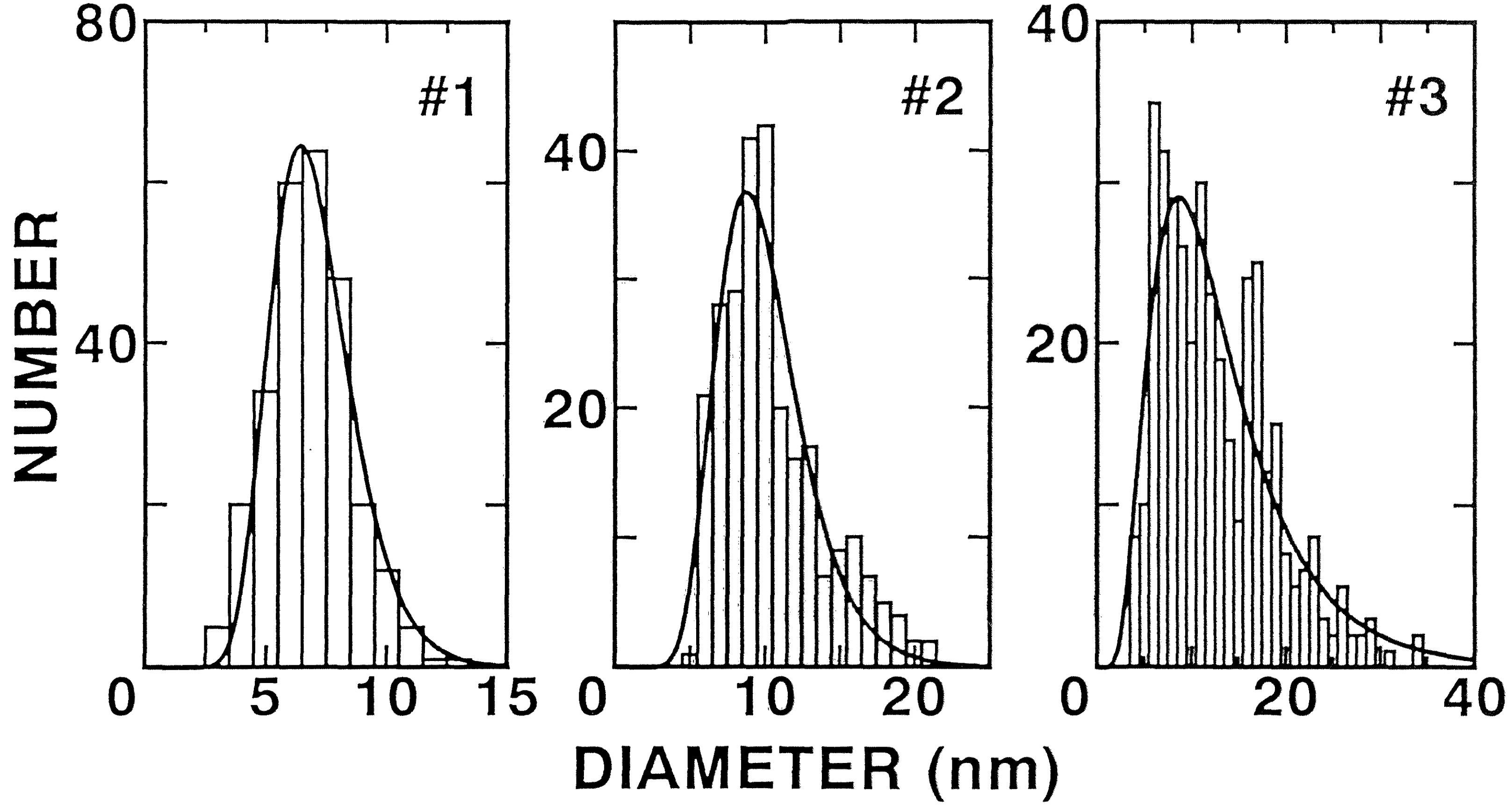

Fig. 7.2. The size distributions of Si nanocrystals. The solid curves show log–normal distribution function fitted to the data. The average diameters were fitted to be 7.0, 10.0, and 13.3 nm for the samples #1, #2, and #3, respectively.

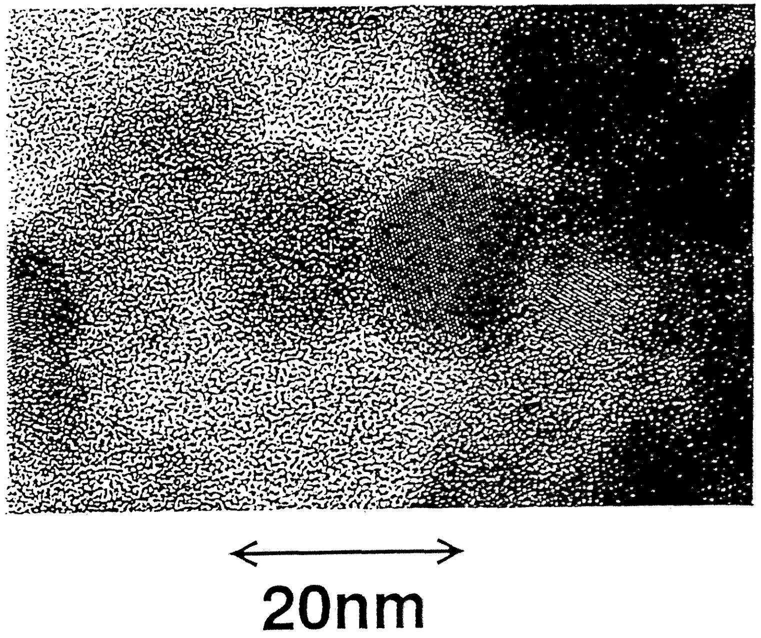

Fig. 7.3. High-resolution TEM image of Si nanocrystals of #1. The lattice fringes can be clearly seen and the nanocrystals are covered by oxide layers. The average thickness of the oxide layer is 1.6 nm.

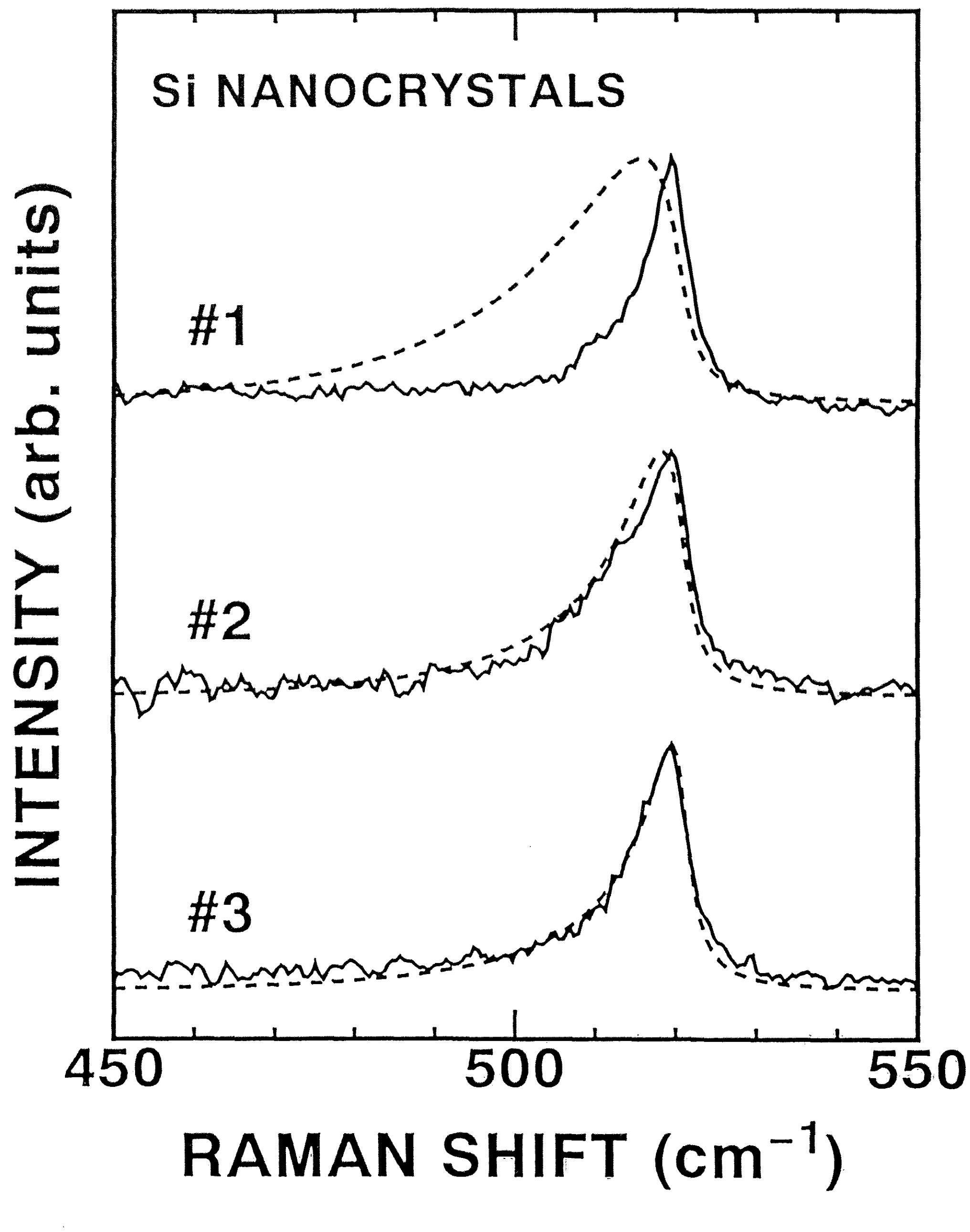

Fig. 7.4. Raman scattering spectra of Si nanocrystals. The broken lines show the calculated Raman spectra using the SC model and the LO phonon dispersion curve.

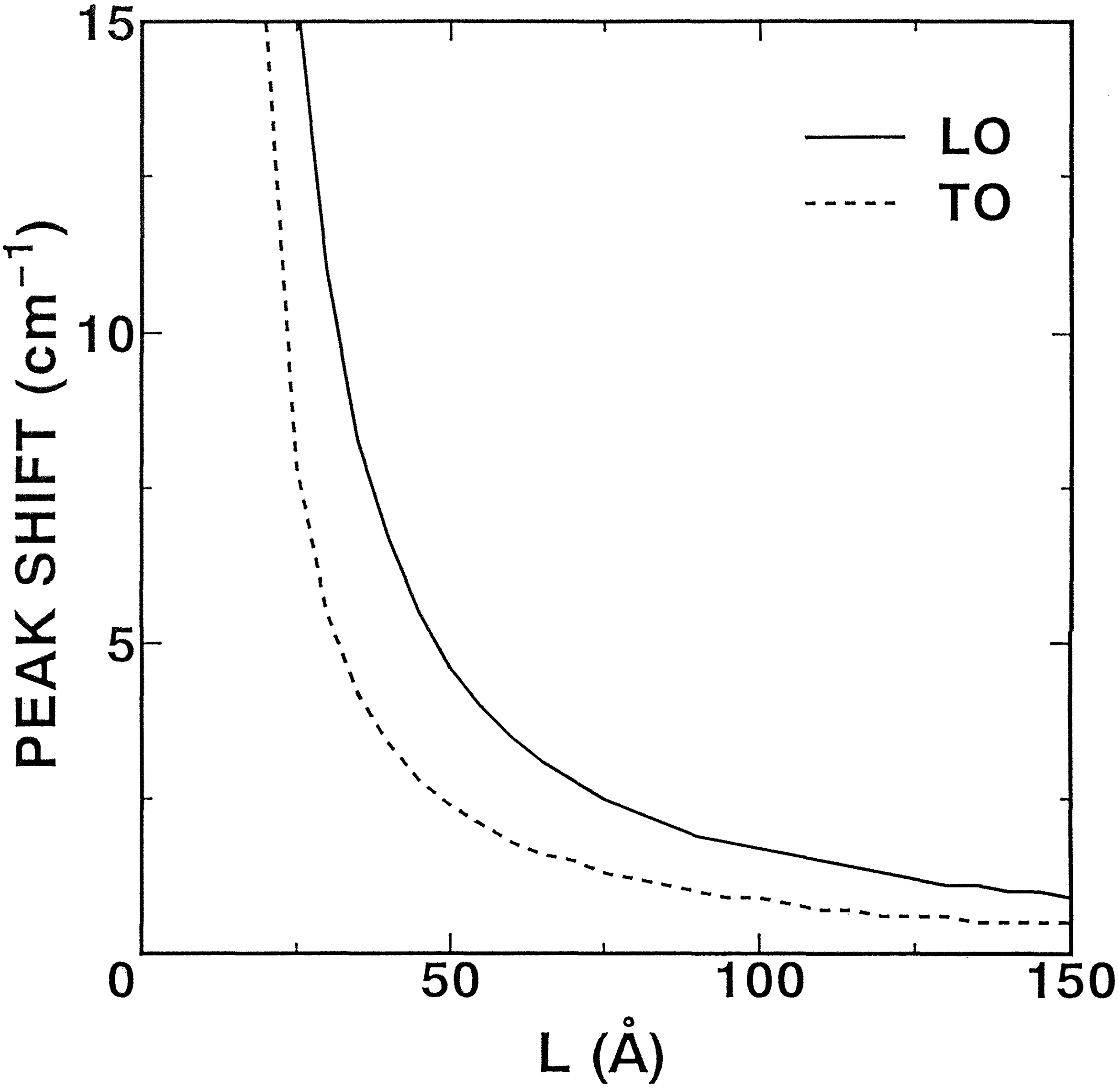

Fig. 7.5. The energy shifts from the bulk Si energy (521 cm^{-1}) as a function of the diameter of Si nanocrystals, L, calculated using the SC model. The solid and broken lines correspond to LO and TO phonon modes, respectively. It shows that with decreasing the nanocrystal size, the energy difference between LO and TO modes increases.

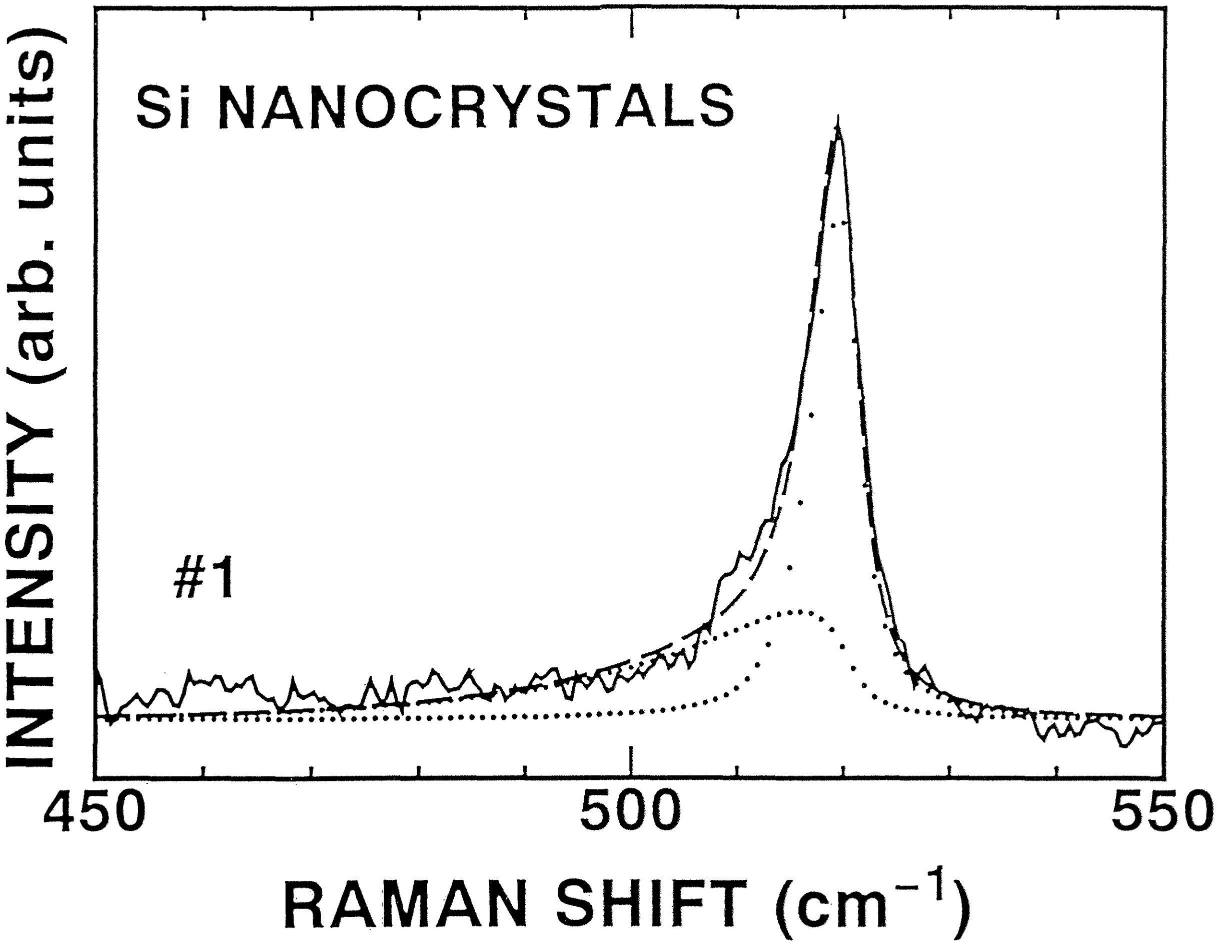

Fig. 7.6. Raman spectrum of sample #1. We fit the spectrum by superposing the LO phonon spectrum on the weakly-confined TO phonon spectrum (dotted lines). The broken line shows the fitted spectrum.

CHAPTER VIII

CONCLUSION

In this thesis, Raman scattering in semiconductor nanostructures, especially heterostructures and nanocrystals, were studied. We used ZnSe–ZnS strained–layer superlattices (SLSs), $Si_{0.5}Ge_{0.5}/Ge/Si_{1-x}Ge_x$ heterostructures, and Si nanocrystals. By using macro– and micro–Raman scattering spectroscopy, zone–folded modes of acoustic phonons, stress effect on the optical phonons, and the confinement of optical phonons were studied. The results and conclusions are summarized as follows.

Higher–order (up to the 5th order) zone–folded modes were observed in ZnSe–ZnS strained–layer superlattices (SLSs) whose average lattice constant is equal to that of a GaAs substrate. We were able to reproduce the zone–folded spectrum using TEM data and a photoelastic model. The agreement between our calculation and the measurement shows that the Raman spectrum reflects dominantly the periodicity of the superlattices and the roughness of the interface. Furthermore, the stress does not play an important role to the observation of the zone–folded modes.

Next, we studied the optical phonons in ZnSe–ZnS SLSs. In these heterostructures, there exists a strain lying in the plane parallel to the interface. In order to investigate the directional stress, we newly measured Raman scattering with the incident light parallel as well as perpendicular to the interface plane. As a result, we observed for the first time two types of the optical phonon shifts, a singlet and a doublet, induced by the biaxial stress. We obtained reasonable relations between the stress and the direction of the shift and between the layer thickness and the shift. The singlet–type mode shifts larger than the doublet–type mode for the ZnSe optical phonon modes. These experimental results were explained theoretically. The method of this work will become a new characterization tool for evaluating the directional stress in these heterostructures.

We studied the Raman scattering from the submicron–order region of $Si_{0.5}Ge_{0.5}/Ge/Si_{1-x}Ge_x$ heterosturctures. Generally, the spatial resolution is thought to be limited by the spot size of the laser beam at the sample surface. The spot size is about 1 μm when the micro–Raman measurement system is used. Whereas, we measured the Raman scattering in $Si_{0.5}Ge_{0.5}/Ge/Si_{1-x}Ge_x$ heterostructures by scanning the irradiated spot at intervals of ~0.1 μm and obtained submicron–order profile of Raman spectra. The calculations which consider the beam profile (Gaussian shape) and the structural profile fully reproduced the dependence of the Raman intensity on the position of the irradiated spot. The results suggest that if we consider the beam profile, we can observe the Raman signal from the submicron–order region of the opaque sample.

Finally, we studied the confinement effect of optical phonons in Si nanocrystals fabricated by a gas break–down method. The Raman spectrum of the smallest nanocrystals showed the high energy peak shift and the narrowing of the spectral width. These anomalous behaviors can be explained by the spatial correlation (SC) model which considers both the dispersion curves of LO and TO phonons. It was shown that as the size of nanocrystals decreases, the energy difference between LO and TO phonons increases, the LO phonon mode becomes broad and weak, and TO phonon mode becomes dominant. Our treatment of the confinement of optical phonons also reasonably explained the previous experimental results of the other authors.

As mentioned above, we have discussed the properties of phonons in semiconductor nanostructures by using Raman scattering spectroscopy. In closing this work, we would like to assert that Raman scattering spectroscopy is a powerful tool to investigate the lattice dynamics in semiconductor nanostructures.

ACKNOWLEDGEMENTS

The author express a deep sense of gratitude to Professor Y. Masumoto of University of Tsukuba for his constant guidance and encouragement throughout this work. He wishes to express his sincere thanks to Dr. Y. Kanemitsu of University of Tsukuba for the continuing suggestions and encouragement and to Dr. T. Mishina of University of Tsukuba for the fruitful discussions and advice.

The author would like to express his appreciation to Prof. S. Nakashima and his coworkers of Osaka University for their instruction of the basic technique of Raman scattering experiments and for their helpful discussions.

The Raman scattering experiments were done at the Cryogenic Center, University of Tsukuba. The author wishes to acknowledge Prof. R. Yoshizaki and technical officers of the Cryogenic Center for their kind help of his Raman scattering experiments.

The author is much indebted to Y. Yamada of University of Tsukuba for his kindly providing the samples and collaboration. He also wishes to acknowledge Dr. S. Yamaga and Prof. A. Yoshikawa of Chiba University, K. Nakagawa of Hitachi Ltd., and T. Kawaguchi and S. Miyazima of JVC Co., Ltd. for their kindly providing the samples.

The author is indebted to K. Nagao of Fuji Photo Film Co., Ltd. for acquiring two-dimensional densitometric data of TEM images and to S. Nagata of Mechanical Engineering Laboratory for his help in the computer programs.

Finally, the author would like to thank all the members of the research group of Prof. Masumoto, especially Prof. L. Zimin and Dr. F. Sasaki, for their kind help and encouragements.

This work was partially supported by Hosokawa Powder Technology Foundation.

APPENDIX

In the presence of a strain the dynamical equations for the q=0 optical modes in diamond- or zincblende-type crystals, to terms linear in the strain, has the form[1,2]

$$m\ddot{u}_i=-\sum_k K_{ik}u_k=-\left(K_{ii}^{(0)}u_i+\sum_{klm}\frac{\partial K_{ik}}{\partial\varepsilon_{lm}}\varepsilon_{lm}u_k\right), \tag{A.1}$$

where u_i is the *i*th component of the relative displacement of the two atoms in the unit cell, m is the reduced mass of the two atoms, $K_{ii}^{(0)}=m\omega_0^2$ is the effective spring constant in the absence of strain, and i, k, l, and m denote x or y or z. The last term of Eq. (A.1) is the change in spring constant due to an applied strain ε_{lm}:

$$\frac{\partial K_{ik}}{\partial\varepsilon_{lm}}\varepsilon_{lm}=K^{(1)}_{ik,lm}\varepsilon_{lm}=K^{(1)}_{ik,ml}\varepsilon_{ml}. \tag{A.2}$$

From the thermodynamic and symmetry considerations it can be shown that for cubic crystal there are only three independent components of the tensor $K^{(1)}$, namely,[3]

$$\begin{aligned}K^{(1)}_{xx,xx}&=K^{(1)}_{yy,yy}=K^{(1)}_{zz,zz}=mp,\\ K^{(1)}_{xx,yy}&=K^{(1)}_{yy,zz}=K^{(1)}_{zz,xx}=mq,\\ K^{(1)}_{xy,xy}&=K^{(1)}_{yz,yz}=K^{(1)}_{zx,zx}=mr.\end{aligned} \tag{A.3}$$

From Eq. (A.1) and the above considerations one obtains the following secular equation whose solutions yield the frequencies of the optical phonons in the presence of strain:

$$\begin{vmatrix} p\varepsilon_{xx}+q(\varepsilon_{yy}+\varepsilon_{zz})-\lambda & 2r\varepsilon_{xy} & 2r\varepsilon_{xz}\\ 2r\varepsilon_{xy} & p\varepsilon_{yy}+q(\varepsilon_{zz}+\varepsilon_{xx})-\lambda & 2r\varepsilon_{yz}\\ 2r\varepsilon_{xz} & 2r\varepsilon_{yz} & p\varepsilon_{zz}+q(\varepsilon_{xx}+\varepsilon_{yy})-\lambda\end{vmatrix}=0, \tag{A.4}$$

where $\lambda=\Omega^2-\omega_0^2$ and Ω is the strain-dependent frequency of the optical phonons and can be assumed as $\Omega \approx \omega_0 + \lambda/2\omega_0$. The relation between the strain tensor [ε] and stress tensor [X] can be written as

$$[\varepsilon]=[S][X], \tag{A.5}$$

where [S] is the compliance tensor. When the biaxial stress is lying parallel to the (001) surface, we can obtain two types of the energy deviations from the energy of bulk modes:

$$\begin{aligned}\Delta\Omega_s &= [pS_{12}+q(S_{11}+S_{12})]X/\omega_0, \\ \Delta\Omega_d &= [p(S_{11}+S_{12})+q(S_{11}+3S_{12})]X/2\omega_0,\end{aligned} \tag{2.24}$$

where $\Delta\Omega_s$ indicates the shift of the singlet-type mode vibrating parallel to the <001> axis, while $\Delta\Omega_d$ indicates the shift of doublet-type modes vibrating perpendicular to the <001> axis.

References

[1] E. Anastassakis, A. Pinczuk, E. Burstein, F. H. Pollak, and M. Cardona, Solid State Commun. **8**, 133 (1970).

[2] F. Cerdeira, C. J. Buchenauer, F. H. Pollak, and M. Cardona, Phys. Rev. B **5**, 580 (1972).

[3] S. Ganesan, A. A. Maradudin, and J. Oitmaa, Ann. Phys. (N. Y.) **56**, 556 (1970).

LIST OF PUBLICATIONS

[1] "*Biaxial Splitting of Optical Phonon Modes in ZnSe-ZnS Strained-Layer Superlattices,*"

A. Yamamoto, Y. Yamada, and Y. Masumoto:

Appl. Phys. Lett. **58**, 2135 (1991).

[2] "*Raman Study of Disorder and Strain in Epitaxial* ZnS_xSe_{1-x} *films on a GaAs Substrate,*"

Y. Kanemitsu, A. Yamamoto, H. Matsue, Y. Masumoto, S. Yamaga, and A. Yoshikawa:

Appl. Phys. Lett. **60**, 1330 (1992).

[3] "*Residual Strains and Disorder in ZnSSe Epitaxial Films on GaAs,*"

Y. Kanemitsu, A. Yamamoto, H. Matsue, H. Nabeta, Y. Masumoto, S. Yamaga, A. Yoshikawa, K. Yamanaka, Y. Nagata, and T. Koda:

J. Cryst. Growth, **117**, 316 (1992).

[4] "*New Characterization Method of Biaxial Stress by Raman Scattering: Demonstration in ZnSe-ZnS Strained-Layer Superlattices,*"

A. Yamamoto, Y. Yamada, and Y. Masumoto:

J. Cryst. Growth, **117**, 488 (1992).

[5] "*Photoacoustic Characterization of Semiconductor Heterostructures,*"

Y. Kanemitsu, H. Nabeta, H. Matsue, A. Yamamoto, Y. Nagata, K. Yamanaka, T. Koda, and Y. Masumoto:

Jpn. J. Appl. Phys. **31**, suppl. 31-1, 29 (1992).

[6] "*Higher Order Zone-Folded Modes in ZnSe-ZnS Strained-Layer Superlattices*," A. Yamamoto, Y. Kanemitsu, Y. Masumoto, S. Yamaga, and A. Yoshikawa: Appl. Phys. Lett. **61**, 1700 (1992).

Other Fields

[7] "*Construction of Millimeter- and Submillimeter-Wave Interferometric Spectrometer and Its Application to Measurements of Optical Constants*," S. Nakashima, T. Hattori, M. Hangyo, A. Yamamoto, K. Sakai, A. Mitsuishi, and S. Hashimoto: Oyo Buturi, **59**, 1093 (1990), in Japanese.

[8] "*Photocarrier Generation in Metal-Free Phthalocyanines: Effect of the Stacking Habit of Molecules on the Photogeneration Efficiency*," Y. Kanemitsu, A. Yamamoto, H. Funada, and Y. Masumoto: J. Appl. Phys. **69**, 7333 (1991).